Titanite-bearing calc-silicate rocks constrain timing, duration and magnitude of metamorphic CO2 degassing in the Himalayan belt

UNIVERSITÀ DEGLI STUDI DI TORINO

TITANITE-BEARING CALC-SILICATE ROCKS CONSTRAIN TIMING, DURATION AND MAGNITUDE OF METAMORPHIC CO_2 DEGASSING IN THE HIMALAYAN BELT

Giulia Rapa[a], Chiara Groppo[a,b,*], Franco Rolfo[a,b], Maurizio Petrelli[c], Pietro Mosca[b], Diego Perugini[c]

[a]Department of Earth Sciences, University of Torino, Via Valperga Caluso 35, 10125 Torino, Italy

[b]IGG-CNR, Via Valperga Caluso 35, 10125 Torino, Italy

[c]Department of Physics and Geology, University of Perugia, Piazza Università, 06100 Perugia, Italy

*Corresponding Author

Chiara Groppo

Dept. of Earth Sciences, University of Torino

Via Valperga Caluso, 35 – 10125 Torino, Italy

Tel. +39 0116705106

Fax +39 0116705128

Abstract

The pressure, temperature, and timing (P-T-t) conditions at which CO_2 was produced during the Himalayan prograde metamorphism have been constrained, focusing on the most abundant calc-silicate rock type in the Himalaya. A detailed petrological modelling of a clinopyroxene + scapolite + K-feldspar + plagioclase + quartz ± calcite calc-silicate rock allowed the identification and full characterization - for the first time – of different metamorphic reactions leading to the simultaneous growth of titanite and CO_2 production. The results of thermometric determinations (Zr-in-Ttn thermometry) and U-Pb geochronological analyses suggest that, in the studied lithology, most titanite grains grew during two nearly consecutive episodes of titanite formation: a near-peak event at 730-740°C, 10 kbar, 30-26 Ma, and a peak event at 740-765°C, 10.5 kbar, 25-20 Ma. Both episodes of titanite growth are correlated with specific CO_2-producing reactions and constrain the timing, duration and P-T conditions of the main CO_2-producing events, as well as the amounts of CO_2 produced (1.4-1.8 wt% of CO_2). A first-order extrapolation of such CO_2 amounts to the orogen scale provides metamorphic CO_2 fluxes ranging between 1.4 and 19.4 Mt/yr; these values are of the same order of magnitude as the present-day CO_2 fluxes degassed from spring waters located along the Main Central Thrust. We suggest that these metamorphic CO_2 fluxes should be considered in any future attempts of estimating the global budget of non-volcanic carbon fluxes from the lithosphere.

Key-words

Calc-silicate rock; metamorphic CO_2 production; Himalayan orogeny; Zrn-in-titanite thermometry; U-Pb geochronology; non-volcanic carbon fluxes

1. Introduction

Metamorphic degassing from active collisional orogens supplies a significant fraction of CO_2 to the atmosphere, playing a key role in the long-term (> 1 Ma) global carbon cycle (e.g. Bickle, 1996; Evans, 2011; Gaillardet and Galy, 2008; Skelton, 2011). Primary geologic settings for the production of significant amounts of metamorphic CO_2 include "large-hot" collisional orogens, where decarbonation reactions occur at a relatively high temperature within carbonate-bearing metasediments (e.g. calc-silicate rocks), in which metamorphic reactions between carbonates and silicates trigger CO_2 production.

Being the most prominent recent and still active "large-hot" orogen on Earth, the Himalayan belt is the best candidate for the generation of a significant amount of metamorphic CO_2 during the Cenozoic. Previous studies aimed at quantifying metamorphic CO_2 degassing in the Himalayas yield conflicting results and argued either in favour of a significant contribution to periods of greenhouse global warming in the past (Becker et al., 2008; Kerrick and Caldeira, 1993), or against it (Kerrick and Caldeira, 1998, 1999; Selverstone and Gutzler, 1993). The nature and magnitude of the metamorphic CO_2 cycle in the Himalaya, however, is still poorly known because, as pointed out by Kohn and Corrie (2011), Himalayan calc-silicate rocks have been largely ignored in previous metamorphic studies. Major uncertainties are: (1) the volumes of CO_2-source rocks and their relevant mineral assemblages; (2) the nature of the metamorphic CO_2-producing reactions; (3) the P-T conditions at which the decarbonation reactions took place; (4) the timing and duration of CO_2-producing events, which is essential for understanding whether the Himalayan orogeny was responsible for ancient periods of global warmth and for estimating the annual mass flux of CO_2 released during these periods.

Concerning point (1), although calc-silicate rocks in the metamorphic core of the Himalaya (i.e. in the Greater Himalayan Sequence: GHS) have been reported since the pioneering works of

68 Bordet (1961), Gansser (1964) and Le Fort (1975), a systematic study of the different types of calc-
69 silicate rocks and of their distribution within the GHS has been undertaken only recently (Rolfo et
70 al., 2015, 2017). Point (2) has also been a major focus of recent studies (Groppo et al., 2013,
71 2017): devolatilization reactions in different types of Himalayan calc-silicate rocks have been
72 investigated using a novel approach which combines phase diagram modelling with a detailed
73 interpretation of microstructures. New CO_2-producing reactions have been recognised, involving
74 Ca-Mg-Fe- (garnet, clinopyroxene) and Ca-Na- (plagioclase, scapolite) solid solutions, as well as K-
75 bearing phases (biotite, muscovite, K-feldspar). Groppo et al. (2017) also provided preliminary
76 insights on point (4) by demonstrating that, in internally buffered systems, CO_2 is mainly produced
77 at isobaric invariant points, thus suggesting that the duration of the CO_2-producing events is
78 significantly shorter than the duration of prograde metamorphism.

79 This work focuses on points (3) and (4), i.e. on the still vague estimate of both the P-T
80 conditions and the timing of CO_2-producing events which occurred during Himalayan prograde
81 metamorphism. The P-T conditions experienced by calc-silicate rocks can be indirectly estimated
82 using associated metapelites (e.g. Groppo et al., 2013, 2017). As a drawback, indirect P-T
83 estimations provide only qualitative knowledge about the timing of the events. Alternatively, the
84 recently calibrated trace element thermometer based on the zirconium content in titanite (Zr-in-
85 Ttn: Hayden et al., 2008) is a promising method to directly constrain the thermal history of calc-
86 silicate rocks, because titanite is a common accessory mineral in these lithologies and the Zr-in-Ttn
87 thermometer is independent of $X(CO_2)$ in the fluid. Titanite's slow Zr diffusivity permits retention
88 of Zr-temperatures up to at least 750-775 °C (Cherniak, 2006; Kohn and Corrie, 2011; Walters and
89 Kohn, 2017; see also Kohn, 2016, 2017 for a review). The Zr-in-Ttn thermometer is, therefore,
90 applicable to calc-silicate rocks from the GHS, which experienced peak temperatures $\leq$ 800°C (e.g.
91 Groppo et al., 2013, 2017; Kohn and Corrie, 2011). A further advantage of titanite is that it can also

92 be used as a chronometer (e.g. Frost et al., 2000; Kohn, 2017), thus linking U-Pb ages with
93 temperatures through simultaneous geochronology and trace element thermometry in single
94 microanalytical spots. Recent petrochronological studies have demonstrated that Pb diffusivity in
95 titanite is very slow (e.g. Kohn and Corrie, 2011; Gao et al., 2012; Spencer et al., 2013; Stearns et
96 al., 2015; Walters and Kohn, 2017). As a consequence, titanite crystals act as recorders of their
97 prograde growth at high temperature. Few studies have already successfully obtained titanite U-
98 Pb ages from Himalayan calc-silicate rocks and other Himalayan lithologies (e.g. Cottle et al., 2011;
99 Kohn and Corrie, 2011; Warren et al., 2012; Walters and Kohn, 2017). However, although well
100 constrained in term of T and P, the titanite ages obtained so far are still not related to specific CO_2-
101 producing events.
102 The aim of this work is to constrain the P-T-t conditions at which CO_2 was produced during
103 the Himalayan orogeny, focusing on the most abundant calc-silicate type in the Himalayas (i.e.
104 clinopyroxene + scapolite + K-feldspar + plagioclase ± calcite calc-silicate rocks; Rolfo et al., 2017).
105 Metamorphic reactions that led to the simultaneous growth of titanite and production of CO_2 are
106 identified and fully characterized for the first time. T-t data from different titanite generations are
107 correlated with specific CO_2-producing reactions, allowing constraining the timing, duration and P-
108 T conditions of the main CO_2-producing events, as well as the amounts of CO_2 produced;
109 furthermore, a first order extrapolation of these CO_2 amounts to the orogen scale is proposed.
110
111 ## 2. Sample description
112 ### *2.1 Geological setting*
113 The studied sample 14-53c was collected from a calc-silicate level (~ 2 m -thick) embedded within
114 metapelitic gneisses of the Lower Greater Himalayan Sequence (L-GHS), in the Gosainkund-
115 Helambu region of central Nepal (N28°00'37.3'', E85°29'50.9''; 3365 m a.s.l.; Fig. 1a,b). In this area,

116 the L-GHS is bounded at its bottom by the Main Central Thrust (MCT), which juxtaposes the L-GHS
117 onto the Lesser Himalayan Sequence (LHS), and at its top by the Langtang Thrust (LT: Kohn, 2008;
118 Kohn et al., 2005), which juxtaposes the Upper GHS unit (U-GHS) onto the L-GHS. Both the L-GHS
119 and the U-GHS are thick metasedimentary sequences consisting of medium- to high-grade
120 metapelites with calc-silicate layers and bodies of granitic orthogneisses. Metamorphic grade
121 increases upward, reaching anatexis in the structurally higher levels of the L-GHS and in the U-
122 GHS. The structural and lithological features of the area are described in detail by Rapa et al.
123 (2016). The metapelitic gneisses hosting the studied sample experienced peak P-T conditions of
124 720-760 °C, 9-10 kbar (e.g. sample 14-52: Rapa et al., 2016).
125 Sample 14-53c was chosen because it is representative of the most abundant calc-silicate
126 type in the GHS, which occurs as tens to hundreds of meter thick layers in the U-GHS and as
127 thinner (few meters to tens of meters thick) layers in the L-GHS (Rolfo et al., 2015, 2017). These
128 calc-silicate gneisses belong to the complex group of metacarbonate rocks, ranging in composition
129 from almost pure marble to carbonate-free lithologies (Fig. SM1). They derive from nearly
130 isochemical regional metamorphism of former marly protoliths (Fettes and Desmons, 2007),
131 whose main components were clay minerals (smectite, illite, kaolinite and/or chlorite), carbonates
132 (mainly calcite) and quartz. Depending on the primary amount of carbonates, decarbonation
133 reactions which occurred during prograde metamorphism can have led to the partial or total
134 consumption of the original carbonate minerals, as observed in the calcite-poor domains of the
135 studied sample (see Section 2.2). The sample was collected far from structures that can potentially
136 represent preferential pathways for the entrance of external fluids (e.g. fold hinges, shear zones,
137 faults, veins).
138
139 ***2.2 Petrography and mineral chemistry***

140 The calc-silicate level from which the studied sample was collected shows a banded structure,
141 being characterized by dm-thick layers with different mineral assemblages (Fig. 1c). These layers
142 consist of: quartz + clinopyroxene + calcic plagioclase (sample 14-53a); garnet + calcic plagioclase +
143 clinopyroxene + epidote (14-53b); quartz + clinopyroxene + calcic plagioclase + K-feldspar +
144 scapolite ± calcite (14-53c); quartz + garnet + scapolite + clinopyroxene + calcic plagioclase (14-
145 53d). The studied sample 14-53c is a fine-grained calc-silicate rock with a granoblastic texture, in
146 which calcite-rich domains alternate with calcite-poor domains, defining a cm-thick layering (Fig.
147 2). The main mineral assemblage in both domains consists of quartz + clinopyroxene + calcic
148 plagioclase + K-feldspar + scapolite ± calcite, minor epidote, biotite and titanite, and accessory
149 bluish tourmaline and zircon; the modal proportion of the mineral phases is different in the two
150 domains (Table 1a and Fig. 2). Representative microstructures and mineral chemical data are
151 reported in Fig. 3-6. Mineral abbreviations are according to Whitney and Evans (2010).

152 K-feldspar (Or_{95-100}) in both domains includes quartz, rare scapolite and clinopyroxene (Fig.
153 3b-c), and is locally included in plagioclase (Fig. 4b,i); myrmeckitic microstructures are observed at
154 the interface with plagioclase. In the Cal-rich layers, K-feldspar is locally included in biotite (Fig.
155 3a), showing corroded margins against it. Triple junctions between K-feldspar and scapolite are
156 observed in the matrix. Clinopyroxene (Di_{64-67}) is pale green and occurs as mm-sized granoblasts.
157 The clinopyroxene core contains rare small mono- and polymineralic inclusions of amphibole
158 (mostly actinolite with X_{Mg}=0.65-0.90) + calcite + quartz + titanite + biotite with corroded margins,
159 while the rim includes mono-mineralic inclusions of quartz, scapolite, titanite and K-feldspar (Fig.
160 3d-f). Clinopyroxene is rarely included in plagioclase in both domains (Fig. 4b,c).

161 Plagioclase (An_{90-97}) mainly occurs as medium-grained granoblasts. In the Cal-poor
162 domains, plagioclase often includes vermicular quartz and mono-mineralic inclusions of scapolite,
163 K-feldspar, and rare epidote (Fig. 4a,i). In the Cal-rich layers it includes rounded calcite, scapolite,

clinopyroxene, K-feldspar, and quartz (Fig. 4b-d). A less calcic plagioclase (An_{73-78}) is rarely preserved as relict inclusions in scapolite and titanite (Fig. 4e & 5b). Plagioclase is locally surrounded by a rim of epidote in the Cal-poor domains (Fig. 4i), and of epidote + calcite in the Cal-rich domains. Scapolite in the matrix ranges from $eqAn_{61-68}$ in the Cal-poor domains, to $eqAn_{45-68}$ in the Cal-rich domains and contains some Cl (0.31-1.55 wt%). Matrix scapolite includes quartz, rare relict plagioclase (An_{73-78}) (Fig. 4e) and titanite, and is locally partially replaced by symplectitic aggregates of epidote + quartz ± calcite (Fig. 4g,h). Scapolite included in K-feldspar, plagioclase, and clinopyroxene, has a composition in the range $eqAn_{64-75}$ (equivalent anorthite content, eqAn = (Al-3)/3); a few inclusions in titanite (Fig. 5f) show lower eqAn values ($eqAn_{48}$).

Biotite (X_{Mg}=0.57-0.66; Ti=0.04-0.06 a.p.f.u.) in the matrix occurs as deformed lamellae with corroded margins; it is locally included in clinopyroxene and titanite (Fig. 3f & 5d-f), with lobate and rounded margins against the hosting mineral. Epidote included in plagioclase is a Zo_{65}. Epidote forming the symplectitic aggregates replacing scapolite is locally zoned, with a Zo_{57-63} core and a Zo_{81} rim. Epidote replacing plagioclase and clinopyroxene is a Zo_{61-79}.

Calcite is almost pure, with small amounts of Fe (0.01-0.02 a.p.f.u.) and Mg (0.01 a.p.f.u.). In both Cal-poor and Cal-rich domains, calcite is preserved as inclusion within clinopyroxene (in association with amphibole and quartz, Fig. 3d) and titanite (Fig. 5c,d); in the Cal-rich domains, it is also included in plagioclase (Fig. 4d). Calcite granoblasts in the matrix occur only in Cal-rich domains, where they locally overgrow scapolite (Fig. 4f).

3. Methods

3.1 Whole-rock microstructural and mineral chemical characterization

Qualitative major element X–ray maps of the entire thin section were acquired using a micro-XRF Eagle III–XPL spectrometer equipped with an EDS Si(Li) detector and with an EdaxVision32

188 microanalytical system at the Department of Earth Sciences, University of Torino. The operating
189 conditions were 100 ms counting time, 40 kV accelerating voltage and a probe current of 900 μA.
190 A spatial resolution of about 65 μm in both x and y directions was used. Quantitative modal
191 amounts of each mineral phase were obtained by processing the μ-XRF maps with the software
192 program Petromod (Cossio et al., 2002).

193 The rock-forming minerals were analysed with a Jeol JSM-IT300LV Scanning Electron
194 Microscope equipped with an energy dispersive spectrometry (EDS) Energy 200 system and an
195 SDD X-Act3 detector (Oxford Inca Energy) at the Department of Earth Sciences, University of
196 Torino. The operating conditions were 50 s counting time and 15 kV accelerating voltage. SEM-EDS
197 quantitative data (spot size 2 μm) were acquired and processed using the Microanalysis Suite Issue
198 12, INCA Suite version 4.01; natural mineral standards were used to calibrate the raw data; a ϕρZ
199 correction was applied.

200 The bulk rock compositions of the Cal-poor and Cal-rich domains were calculated by
201 combining the mineral proportions obtained from the quantitative modal estimate of the micro-
202 XRF maps (see above) with mineral chemistry acquired with the SEM–EDS and are given in Table 2.
203 The fine-grained nature of epidote hampered its discrimination in the micro-XRF map. Therefore,
204 its (low) modal amount was estimated visually.

205

206 ***3.2 Titanite textural, chemical and isotopic characterization***

207 The textural relationships between titanite and the other minerals, as well as the major element
208 composition of titanite, were investigated by SEM (same equipment used for analysing the main
209 rock-forming minerals; see section 3.1). Titanite is abundant in both Cal-poor and Cal-rich layers; it
210 often includes scapolite, quartz and biotite, and less frequently plagioclase (An_{73-94}), K-feldspar,
211 calcite, epidote and apatite (Fig. 5a-f). Titanite crystals are commonly 100 to 250 μm in length and

20 to 100 μm in width. Most of the analyzed titanite grains are dispersed in the rock matrix; a few analyses have been performed on titanite grains included in clinopyroxene and scapolite. Titanite shows a patchy zoning, as already observed by other authors (e.g. Franz and Spear, 1985; Hayden et al., 2008; Kohn and Corrie, 2011; Kohn, 2017).

In situ trace element analyses and U/Pb age determinations of titanite samples were performed by Laser Ablation Inductively Coupled Plasma Mass Spectrometry (LA-ICP-MS) at the Department of Physics and Geology, University of Perugia (Petrelli et al., 2016). The LA-ICP-MS system was a G2 Teledyne Photon Machine ArF excimer (193 nm) LA system coupled with an iCAPQ Thermo Fisher Scientific, quadrupole based, ICP-MS. LA-ICP-MS operating conditions were tuned before each analytical session to provide maximum signal intensity and stability for the ions of interest. Oxides formation (ThO/Th < 0.5) and Th/U sensitivity ratio (Th/U ~ 1) were also monitored to maintain robust plasma conditions (e.g. Petrelli et al., 2016). Because of the reduced dimensions of the analysed titanite samples, a laser beam diameter ranging between 30 and 40 μm was utilized. The laser energy on the sample surface and the repetition rate were fixed to 3.5 J/cm^2 and 8 Hz, respectively. In detail, trace elements determinations, performed on the isotopes ^{90}Zr, ^{232}Th and ^{238}U, were calibrated using the NIST SRM 612 glass reference material (Pearce et al., 1997). The OLT1 (Kennedy et al., 2010) and MKED1 (Spandler et al., 2016) titanite reference materials were employed as quality controls for trace element determinations. Data reduction was performed using the IOLITE 3 (Paton et al., 2011) software utilizing the protocol described by Longerich et al. (1996). U/Pb age determinations were performed using the same protocol reported by Chew et al. (2016). The OLT1 (Kennedy et al., 2010) and MKED1 (Spandler et al., 2016) titanite reference materials were employed as calibrator and quality control, respectively. Both U/Pb age determinations and trace element analyses were performed preferably in the most homogeneous portions of each titanite grain, as determined using BSE images. Results on

236 unknown samples are reported in Table 3; results from the quality controls are reported in Tables
237 SM1-SM2 and Fig. SM5.
238
239 ***3.3 Phase diagrams computation***
240 Phase diagrams in the Na_2O-CaO-K_2O-(FeO)-MgO-Al_2O_3-SiO_2-TiO_2-H_2O-CO_2 (NCK(F)MAST–HC)
241 system were calculated using Perple_X (version 6.7.4, November 2016) (Connolly 1990, 2009) and
242 the internally consistent thermodynamic dataset and equation of state for H_2O of Holland and
243 Powell (1998, revised 2004). Fe^{3+} was neglected because Fe^{3+}-rich oxides are absent and the
244 amount of Fe^{3+} in the analysed minerals is very low. All the phase diagrams were calculated along
245 a P/T gradient reflecting the P-T path followed by the hosting metapelites (Rapa et al., 2016).
246 For the calculation of the P/T-X(CO_2) pseudosections in the NCKFMAST-HC system the
247 following solid solution models were used: Holland and Powell (1998) for dolomite, chlorite,
248 garnet and clinopyroxene, Diener and Powell (2012) for amphibole, Tajcmanova et al. (2009) for
249 biotite, Newton et al. (1980) for plagioclase and Kuhn et al. (2005) for scapolite, in addition to the
250 binary H_2O-CO_2 fluid. Calcite, K-feldspar, muscovite, paragonite, margarite, kyanite, quartz,
251 titanite, rutile, ilmenite and zoisite were considered as pure end-members. In the pseudosection
252 modelling, the binary H_2O-CO_2 fluid is considered as a saturated fluid phase.
253 P/T-X(CO_2) grids and P-T mixed-volatile projection were calculated in the NCKMAST-HC
254 system considering the following mineral phases: plagioclase, scapolite and biotite (phlogopite-Ti-
255 biotite) solid solutions (same references as before); activity modified end-members for chlorite,
256 amphibole, clinopyroxene and zoisite, matching the measured compositions (i.e. aClc=0.7;
257 aTr=0.7; aDi=0.7; aZo=0.75); calcite, kyanite, microcline, muscovite, quartz, titanite, rutile and
258 geikielite pure end-members. A binary solution model for H_2O-CO_2 fluid (Connolly and
259 Trommsdorff, 1991) was additionally used for the P-T mixed-volatile projection. Following the

method illustrated in Groppo et al. (2017), dolomite, margarite, garnet, and wollastonite were excluded from the calculation of the P/T-X(CO_2) grids and P-T mixed-volatile projection (but not from the calculation of the P/T-X(CO_2) pseudosections; see above). Corundum was included in the calculation, but the corundum-bearing equilibria are not shown. Calcite and quartz are not considered in excess, thus giving to the modelled P/T-X(CO_2) grids a more general validity.

3.4 Zr-in-Ttn thermometry

Zr-in-Ttn temperatures were estimated using the calibration of Hayden et al. (2008). Pressure was set to 10.0-10.5 kbar, basing on the results of the pseudosection modelling (see section 5.1 and Table 3); these values are in good agreement with peak-P conditions constrained from the hosting metapelites (Rapa et al., 2016) and more generally at the regional scale for the L-GHS (e.g. Kohn, 2014). We assumed $a SiO_2$=1 because quartz is abundant in both the Cal-poor and Cal-rich domains (> 30 vol%); rutile is absent, therefore TiO_2 is undersaturated. $a TiO_2$=0.60 and $a TiO_2$=0.55 were estimated for the Cal-poor and Cal-rich domains respectively, following Ashley and Law (2015) (i.e. the chemical potential of the TiO_2 component, μTiO_2, was calculated with Perple_X at the P-T conditions of interest and for the specific bulk composition of each domain, and converted to $a TiO_2$ according to the expression proposed by Ashley and Law, 2015). It is worth noting that, although these $a TiO_2$ values are lower than that suggested by Corrie and Kohn (2011) and Kohn and Corrie (2011) for similar rutile-absent assemblages (i.e. $a TiO_2$=0.85), they give Zr-in-Ttn temperatures that are consistent with the temperatures constrained independently for both the studied sample and the hosting metapelites, using the phase equilibrium approach. Measurement precision for Zr in titanite propagates to temperature uncertainties < 1°C; uncertainties of ± 0.05 in $a TiO_2$ and ± 0.5 kbar propagate to additional systematic errors of ± 5 °C and ± 6 °C, respectively.

4. Results

4.1 Phase diagram modelling

The titanite-forming, CO_2-producing reactions relevant for the studied sample were modelled following the approach described by Groppo et al. (2017), i.e. by combining three different types of phase diagrams, each one useful to investigate different aspects of the CO_2-producing history: (i) P/T-X(CO_2) grids permit identification and full characterization (i.e. stoichiometric balance) of the complete set of CO_2-producing univariant and invariant equilibria for the selected compositional system (note that the full characterization of such equilibria is hard to be achieved using pseudosections); (ii) P/T-X(CO_2) pseudosections allow us to recognise to which of these total equilibria the studied sample is effectively sensible; (iii) mixed-volatile P-T grids (i.e. P-T projections with fluid of variable composition) permit understanding the role of the invariant equilibria, in the case of internally buffered systems. The main novelty introduced here is the inclusion of TiO_2 in the system, not just for the calculation of the P/T-X(CO_2) pseudosections, but also for the calculation of the P/T-X(CO_2) grids and mixed-volatile P-T projection. In the following, the main results of the P/T-X(CO_2) pseudosection modelling are described (Fig. 7 and Fig. SM3), while detailed description of the P/T-X(CO_2) grids and mixed volatile P-T projection is reported in the Supplementary Material and in the Fig. SM2-SM4.

Two P/T-X(CO_2) pseudosections were calculated in the NCKFMAST-HC system, using the bulk compositions representative of the Cal-poor and Cal-rich domains, respectively (Table 2). The two pseudosections are topologically very similar (Fig. 7 and Fig. SM3). Both the pseudosections are dominated by large tri-variant fields separated by narrow di-variant-fields. Quadri-variant fields appear only at high temperatures or for high values of X(CO_2). Quartz is stable in the whole P/T-X(CO_2) range of interest. On the contrary, carbonate stability fields are limited to specific P/T-X(CO_2) conditions: calcite is stable at X(CO_2)>0.01 for T=400 °C, and at X(CO_2)>0.5 for T=720 °C; in

the Cal-poor domains its stability field is limited at T<750 °C, whereas in the Cal-rich domains it is predicted to be stable at T>800°C. Dolomite is limited to low-T conditions (T<600°C) or to high $X(CO_2)$ values ($X(CO_2)$>0.6). Plagioclase (with variable composition) is stable over most of the P/T-$X(CO_2)$ range of interest, except for a relatively large field at 0.05<$X(CO_2)$<0.55 and T<730 °C. Scapolite is stable in a wide range of P/T-$X(CO_2)$ conditions at $X(CO_2)$>0.05 and T>470 °C, with few differences between the Cal-rich and Cal-poor domains. Zoisite is limited to $X(CO_2)$<0.55 in both domains.

The chlorite stability field is limited to T<480°C, $X(CO_2)$<0.15; amphibole is confined to an even smaller field at T<450°C, $X(CO_2)$<0.02. Clinopyroxene is predicted to be stable at $X(CO_2)$<0.02 for T=400°C, and at $X(CO_2)$<0.45 for T=700 °C. An almandine-rich garnet is predicted to be stable in both the pseudosections at T>730°C and $X(CO_2)$>0.5; in the Cal-rich domains a grossular-rich garnet is also modelled at T>650 °C, $X(CO_2)$<0.15.

At low T, muscovite is stable over a wide range of $X(CO_2)$ (i.e. $X(CO_2)$=0.03-0.97); its stability field extends up to ~ 630 °C. The breakdown of muscovite coincides with the appearance of K-feldspar. Biotite is predicted to be stable in a wide range of P/T-$X(CO_2)$ conditions, but in the Cal-rich domains its stability field is limited at T<730 °C, whereas in the Cal-poor domains it is predicted to be stable at T>800°C. Finally, the rutile stability field is limited at $X(CO_2)$>0.05 for T=400°C and at $X(CO_2)$>0.9 for T=700°C; titanite is stable at lower $X(CO_2)$ conditions for the same T conditions.

The results of P/T-$X(CO_2)$ grids and pseudosections suggest that the Cal-poor and Cal-rich domains are sensitive to the same univariant and invariant equilibria (Fig. 7 and Fig. SM3):

(i) CAST-HC reaction 5 ($Cal + Qz + Rt \rightarrow Ttn + CO_2$), that controls the relative stability of rutile vs. titanite;

(ii) CKAS-HC reaction 7 ($Cal + Mu + Qz \rightarrow Kfs + Zo + H_2O + CO_2$), that marks the appearance of K-

feldspar at $X(CO_2)<0.45$ and the breakdown of muscovite;

(iii) NCAS-HC reactions 14a (Cal + Pl + Zo + CO_2 → Scp + H_2O) and 14b (Scp + Zo + CO_2→ Cal + Pl + H_2O), that control the relative stability of plagioclase, scapolite, zoisite and calcite;

(iv) CKMAST-HC univariant reactions 85, 90 and 94 and invariant point I35. Reactions 90 (Kfs + Tr + Ttn → Bt + Di + Qz + H_2O + CO_2) and 85 (Bt + Cal + Qz → Kfs + Tr + Ttn + H_2O + CO_2) limit the stability field of amphibole at T<450°C, whereas reaction 94 (Bt + Cal + Qz → Di + Kfs + Ttn + H_2O + CO_2) marks the appearance of clinopyroxene at T > 450°C;

(v) NCKAS-HC univariant reaction 107b and invariant points I44 and I44'. Reaction 107b (Cal + Mu + Qz + Scp → Kfs + Pl + H_2O + CO_2) marks the appearance of K-feldspar (and the breakdown of muscovite) at $X(CO_2) > 0.45$;

(vi) NCKMAST-HC univariant reactions 133a and 133b and invariant points I65 and I65'. The Cal-absent reactions 133a (Bt + Qz + Scp → Di + Kfs + Pl + Ttn + Zo + H_2O + CO_2) and 133b (Bt + Qz + Scp + Zo → Di + Kfs + Pl + Ttn + H_2O + CO_2) represent Pl-forming reactions at relatively low values of $X(CO_2)$.

Among these univariant equilibria, reactions 5, 85, 94 and 133 are titanite-forming and CO_2-producing and, except for reaction 5, they involve mineral phases observed in the studied sample (reaction 5 involves rutile as a reactant, which is not observed in the sample). Reactions 85, 94 and 133 are therefore particularly relevant for this study; they emanate from the titanite-bearing invariant points I35, I65 and I65', which correspond to the following "truly" univariant reactions in the P-T mixed-volatile projection (Fig. SM4):

U35: Cal + Kfs + Tr + Ttn → Bt + Di + Qz + F

U65a: Bt + Cal + Pl + Qz + Zo → Di + Kfs + Scp + Ttn + F

U65c: Bt + Cal + Qz + Scp + Zo → Di + Kfs + Pl + Ttn + F,

where F indicates an H_2O-CO_2 fluid whose composition change as a function of P and T [$X(CO_2)$

values are reported in Fig. SM4; e.g. F54 means a H_2O-CO_2 fluid with $X(CO_2) = 0.54$].

4.2 Zr-in-Ttn thermometry and U-Pb data

Al and Ti in the titanite show an inverse correlation and have a bimodal distribution (Al = 0.23-0.28 a.p.f.u., Ti = 0.70-0.76 a.p.f.u. vs. Al = 0.31-0.35 a.p.f.u., Ti = 0.63-0.69 a.p.f.u.); Zr shows a positive correlation with Al, in agreement with the commonly observed substitution of Al and Zr for Ti (e.g. Franz and Spear, 1985; Kohn, 2017). Overall, the Zr content in the analysed titanite grains is relatively high, spanning between 114 and 237 ppm, corresponding to Zr-in-Ttn temperatures of 729-764 °C (± 15 °C) (Table 3). The frequency distribution of Zr-in-Ttn temperatures shows two main peaks at 731-735°C and 741-750°C, suggesting the existence of two different titanite populations crystallized at T<740°C and at T>740°C, respectively (Fig. 8b). The mean values of Zr-in-Ttn temperatures calculated for the two titanite populations have been compared with the Student *t*-test, which confirmed that they are statistically significant (the results of the statistical analysis are reported in Table SM3).

U ranges between 19 and 207 ppm and shows a linear correlation with Zr, except for two titanite grains which are enriched in U compared to the other grains with similar Zr content. A slight correlation between chemical variations (i.e. Zr content) and ages is observed for most of the analysed titanite. Specifically, titanite grains recording higher temperature of crystallisation are, on average, younger than titanite grains crystallized at lower temperatures (Fig. 8a and Table 3). This feature was also observed by Kohn and Corrie (2011) in similar calc-silicate rocks from the U-GHS, but here it is less pronounced. Overall, the thermometric and geochronological data suggest that the studied calc-silicate rock experienced protracted heating from 730-740°C at 30-26 Ma to peak-T of 750-760 °C at 25-20 Ma (Table 3, Fig. 8 and 9). Two U-enriched titanite grains record younger ages (~15 Ma) and are therefore interpreted as related to a retrograde re-

crystallization/re-equilibration event. Zr-temperatures for this retrograde event are poorly constrained, due to the uncertainty in the estimation of pressure; temperatures of ~720°C have been estimated for P = 9 kbar (Table 3).

It is worth noting that the relative distribution of titanite ages is independent from the assumed common Pb composition ($^{207}Pb/^{206}Pb$ = 0.84, following Stacey and Kramers, 1975; however, higher values of common lead such as those used by Kohn and Corrie (2011) for similar calc-silicate rocks (i.e. common Pb $^{207}Pb/^{206}Pb$ = 0.87) would imply slightly older and more spread in absolute ages (Fig. 8c), whereas lower values of common lead would imply younger and more overlapped absolute ages.

5. Discussion

5.1 P/T-X(CO_2) prograde evolution

Most of the observed microstructures reflect either isobaric/isothermal univariant- or invariant-assemblages (i.e. truly-univariant assemblages in the corresponding mixed-volatile P-T projection), thus suggesting that the system remained internally buffered for most of its metamorphic evolution. Moreover, the close similarity between the modal amounts of minerals observed in the Cal-poor and Cal-rich domains and those predicted by the pseudosections (Table 1a), suggests that little or no externally-derived fluid interacted with the rock.

The occurrence of rare amphibole relics preserved in the core of clinopyroxene, tightly constrains the first portion of the P-T-X(CO_2) evolution in the narrow amphibole stability field, which is limited by the univariant equilibria 85 and 90 (Fig. 7 and Fig. SM3). Moreover, microstructural evidence suggests that clinopyroxene cores grew at the expenses of amphibole + calcite ± quartz (Fig. 3d). This microstructure can be explained by the truly univariant reaction U35 (Cal + Kfs + Tr + Ttn $\rightarrow$ Bt + Di + Qz + F; corresponding to the isobaric/isothermal invariant point

I35); the same reaction could also explain the rare occurrence of corroded inclusions of K-feldspar in biotite (Fig. 3a).

Once at least one of the reactants of reaction U35 (i.e. amphibole) was completely consumed, the system evolved along the univariant reaction 94 (Bt + Cal + Qz → Di + Kfs + Ttn + H_2O + CO_2) until it reached the invariant point I65 (i.e. truly univariant reaction U65a: Bt + Cal + Pl + Qz + Zo → Di + Kfs + Scp + Ttn + F). Reaction U65a could explain the rare occurrence of Na-rich plagioclase preserved as corroded inclusions within scapolite and titanite (Fig. 4e & 5b).

The system departed from the invariant point I65 once one of the reactants was totally consumed. Two possibilities can be discussed: (i) calcite was completely consumed, and the system evolved along the univariant reactions 133a and 133b; (ii) Na-rich plagioclase was completely consumed, and the system evolved along the univariant reaction 94. The first possibility is unlikely, because reactions 133a (Bt + Qz + Scp → Di + Kfs + Pl + Ttn + Zo + H_2O + CO_2) and 133b (Bt + Qz + Scp + Zo → Di + Kfs + Pl + Ttn + H_2O + CO_2) would have implied the growth of Na-rich plagioclase, which is instead not observed in the studied sample. Rather, reaction 94 (Bt + Cal + Qz → Di + Kfs + Ttn + H_2O + CO_2) is more likely to have occurred, and it is consistent with the preservation of biotite relics in clinopyroxene (Fig. 3f). The system then evolved along equilibrium 94 until it reached the truly univariant reaction U65c, corresponding to the isobaric/isothermal invariant point I65'. Reaction U65c (Cal + Bt + Scp + Zo + Qz → Cpx + Kfs + Pl + Ttn + F) was responsible for the growth of most of the Ca-rich plagioclase observed in the sample and is consistent with the occurrence of: (i) inclusions of scapolite, epidote and quartz in Ca-rich plagioclase (Fig. 4a); (ii) inclusions of scapolite, biotite, calcite, quartz and epidote in titanite (Fig. 5a,c,d,e,f); (iii) inclusions of biotite, quartz, calcite and scapolite in the clinopyroxene rims (Fig. 3d,e); (iv) inclusions of scapolite in K-feldspar (Fig. 3b).

Once zoisite was exhausted, the system further evolved along the univariant reaction 94. In

Cal-poor domains it is likely that reaction 94 (and its buffering ability) ceased due to the complete consumption of calcite, thus implying that the system entered the Bt + Cpx + Kfs + Pl + Qz + Scp + Ttn stability field that represents the observed peak assemblage. In Cal-rich domains, biotite is probably completely consumed, and the system entered the Cal + Cpx + Kfs + Pl + Qz + Scp + Ttn stability field, in agreement with the observed peak assemblage.

5.2 Different episodes of titanite growth and CO_2 production

5.2.1 P-T-t conditions of titanite growth

It has been demonstrated that, as long as a system remains internally buffered, sudden and volumetrically-significant appearance of new phases and the simultaneous disappearance of previously abundant phases occur at the isobaric/isothermal invariant points, whereas modal changes are only minor along the univariant curves (e.g. Greenwood, 1975; Groppo et al., 2017). In contrast, univariant reactions lead to volumetrically-significant appearance of new phases when the buffering ability of the system ceases due to the complete consumption of one or more reactants.

According to the P-T-X(CO_2) evolution discussed in section 5.1, both the Cal-poor and Cal-rich domains remained internally buffered up to ~740°C, i.e. up to temperatures slightly higher than I65'. At T > 740°C, the buffering ability of both domains ceased due to the complete consumption of calcite/biotite in the Cal-poor/Cal-rich domains, respectively. It follows that, in both domains, the most important episodes of mineral growth/consumption occurred at the invariant points I35, I65, and I65', and at T > 740°C once that calcite/biotite were completely consumed in the Cal-poor/Cal-rich domains, respectively. In more detail, the results of thermodynamic modelling predict three main episodes of titanite growth (Fig. 7, Fig. SM3 and Table 1b): (i) a "prograde" titanite-forming event occurred at ~570°C, 7 kbar (i.e. at I65 through

452 reaction U65a), producing a small amount of titanite; (ii) a “near-peak” event occurred at ~730°C,
453 10 kbar (i.e. at I65’ through reaction U65c) and produced ~0.1/0.2 vol% of titanite in the Cal-
454 poor/Cal-rich domains, respectively; (iii) a “peak” titanite-forming event occurred at conditions of
455 740-765°C, 10.5 kbar through reaction 94, leading to titanite production of ~0.4 vol% in both the
456 Cal-poor and Cal-rich domains.

457 The prediction of thermodynamic modelling is in very good agreement with the Zr-in-Ttn
458 thermometric results, which suggest the existence of two different titanite populations,
459 crystallized at 730-740 °C (“near-peak” event) and 740-765°C (“peak” event), respectively (Fig. 8b).
460 Moreover, the frequency distribution of the measured Zr-temperatures (i.e. “peak” titanite grains
461 are more frequent than “near-peak” titanites) reflects the volume amounts of the two titanite
462 generations as predicted by the thermodynamic modelling (Table 1b). The lack of titanite grains
463 preserving Zr-temperatures of ~570°C suggests a complete re-equilibration/re-crystallization of
464 the prograde generation of prograde titanite during the “near-peak” and/or “peak” events.

465 Although the absolute ages of the two titanite generations are partially overlapped, the
466 “peak” titanite grains are, on average, younger than the “near-peak” titanite grains (Fig. 8a,c and
467 Fig. 9), pointing to ages of 30-26 Ma for the “near-peak” event and of 25-20 Ma for the “peak”
468 event, respectively. These two episodes of titanite growth are also documented by the probability
469 density plot (Fig. 8c).

470

471 *5.2.2 P-T-t constraints on Himalayan prograde metamorphism compared with previous data*

472 Our results suggest that the studied calc-silicate rock from the L-GHS experienced a high-T
473 evolution at T > 730°C for at least 10 Ma (from ~30 to ~20 Ma), followed by a retrograde event at
474 ~15 Ma. The good match between the Zr-temperatures obtained from the analysed titanite grains
475 and the P-T conditions independently estimated for the associated metapelites (Rapa et al., 2016),

476 further confirm the validity of our new P-T data. It is to be noted that peak P-T conditions
477 estimated for the associated metapelites suggest incipient partial melting conditions, i.e. most of
478 the associated metapelites still contain abundant white mica, but show microstructural features
479 (e.g. nanogranites included in garnet) indicative of incipient anatexis (Rapa et al., 2016).

480 Absolute ages obtained for sample 14-53c can be validated against existing monazite
481 chronologic data for the region. Specifically, the prograde evolution of the L-GHS in the Langtang
482 region has been constrained at 35-17 Ma by Kohn et al. (2004, 2005) (early prograde: 37-24 Ma;
483 late prograde: 24-17 Ma), whereas monazite ages younger than ~17 Ma were interpreted as
484 related to final cooling (i.e. melt crystallization). Our titanite ages fit well with these data (Fig. 10),
485 although Kohn et al. (2004, 2005) interpreted both the early prograde and late prograde monazite
486 as sub-solidus phases, thus implicitly assuming that they grew at T < 760°C. However, the same
487 authors (Kohn, 2014) noticed that their interpretation is in contrast with the high Zr-temperatures
488 registered by titanites (Kohn and Corrie, 2011) and discussed the possibility that monazite
489 petrogenesis of core compositions was misinterpreted (e.g., the compositions of monazite cores
490 reflect dissolution-reprecipitation in the presence of melt, not prograde sub-solidus growth).

491 Compared to the geochronological results obtained by Kohn and Corrie (2011) on titanite
492 from U-GHS calc-silicate rocks from the Annapurna region (some tens of km westward of our
493 studied area), our titanites are few million years younger (peak titanite: ~24 Ma vs. ~20 Ma). This
494 is in agreement with the monazite data discussed by Kohn et al. (2004, 2005) and Corrie and Kohn
495 (2011) (summarized in Kohn, 2014), which show that peak metamorphism in the L-GHS was
496 systematically younger than in the U-GHS.

497

498 *5.2.3 Amounts of CO_2 produced and implications for the deep carbon cycle*

499 Both the titanite-forming reactions U65c and 94 are decarbonation reactions and the amount of

500 CO_2 produced through these reactions, as predicted by the P/T-X(CO_2) pseudosections, is of ~0.3
501 wt% and ~1.5 wt% of CO_2 (Fig. 7, Fig. SM3 and Table 1b). These results demonstrate that, during
502 the Himalayan orogeny, CO_2 was produced through distinct, short-lived events, which occurred at
503 specific P-T conditions (see also Groppo et al., 2017). In order to extrapolate the amount of
504 produced CO_2 to the orogen scale, an estimate of the total volume of this type of CO_2-source rocks
505 in the whole Himalayan belt is needed. This is not an easy task, because in most of Himalaya's
506 geological maps calc-silicate rocks are not differentiated from the hosting metapelites. A
507 preliminary estimate of their volume was proposed by Groppo et al. (2017) basing on their own
508 field data from eastern Nepal Himalaya. Here we refine those preliminary estimates by
509 considering additional field data from central-eastern Nepal and literature data from central-
510 western Nepal (Fig. 11). According to these data, calc-silicate rocks similar to those analysed in this
511 study are more abundant in the central and western Nepal Himalaya, where they represent up to
512 ~40 vol% of the whole GHS sequence, than in the eastern Nepal Himalaya, where they represent
513 less than 10 vol% of the whole GHS (~5 vol% on average) (Fig. 11). We therefore consider a
514 conservative (minimum) value of 10 vol% as representative of the total volume of this type of CO_2-
515 source rocks with respect to the whole GHS. The entire volume of GHS rocks that experienced
516 Himalayan metamorphism is approximately ~5 x 10^6 km^3 (considering a strike length of 2500 km,
517 an average thickness of 10 km and an average shortening of 200 km; e.g. Long et al., 2011);
518 consequently, the total volume of the CO_2-source rocks was ~5 x 10^5 km^3. This estimate would
519 result in a total CO_2 production of ~4 x 10^6 and ~2 x 10^7 Mt of CO_2 during the "near peak" and
520 "peak" events, respectively. Although we have demonstrated that CO_2 production occurred in
521 pulses for specific volumes of calc-silicate rocks, extrapolation of the CO_2 flux at the orogen scale
522 should integrate these amounts over the time needed for the entire length of GHS to reach the P-T
523 conditions required for CO_2 production, which can be approximated to ~20 Ma (e.g. Kohn, 2014).

524 This would result in metamorphic CO_2 flux for the "near-peak" and "peak" events of 0.2 and 1
525 Mt/yr, respectively. The lack of field evidence for pervasive carbonation and/or massive graphite
526 precipitation in the lithologies structurally overlying the main calc-silicate layers in the GHS
527 (according to our own observations along transects 5-14 in Fig. 11), suggests that most of the CO_2
528 produced through the investigated metamorphic reactions reached Earth's surface without
529 interacting with the hosting rocks.

530 Sensitivity analysis applied to our estimates (Table 4) shows that the calculated
531 metamorphic CO_2 flux is a minimum estimate. Specifically:

532 (1) CO_2 productivity – The studied calc-silicate rock experienced at least two additional CO_2-
533 producing events: an "early prograde" one at ~430°C, 4 kbar (i.e. at I35 through reaction U35),
534 which released ~0.8 wt% CO_2, and a "prograde" one at ~575°C, 7 kbar (i.e. at I35 through
535 reaction U35), which released ~0.3 wt% CO_2 (Fig. 7 and Fig. SM3, SM4). Summed to the
536 amounts produced at "near peak" and "peak" events, a total production of ~3 wt% CO_2 would
537 result (Table 1b). Furthermore, compared to other samples of the same calc-silicate type, the
538 studied sample is derived from a marly protolith relatively poor in calcite (Fig. S1). It has been
539 demonstrated that the CO_2 productivity of similar calc-silicate rocks derived from Cal-rich marls
540 (see sample 07-22 in Fig. S1) is higher, up to ~5 wt% CO_2 (Groppo et al., 2017). On average, a
541 maximum CO_2 productivity of ~4 wt% CO_2 could be therefore considered for this calc-silicate
542 type.

543 (2) GHS total volume - Other authors proposed larger estimates for the total volume of GHS rocks
544 (e.g. Kerrick and Caldeira, 1999 considered a value of 9×10^5 km^3).

545 (3) Volume of CO_2-source rocks - Our estimate of the volume of this type of CO_2-source rocks is a
546 minimum estimate; a value of 25 vol% could be realistically considered as a maximum
547 estimate.

548 (4) Duration of the CO_2-producing process in the whole GHS - The time needed for the entire
549 length of GHS to reach the P-T conditions required for CO_2 production is poorly constrained. In
550 the sensitivity analysis, we have considered durations of 20 and 30 Ma as minimum and
551 maximum values, respectively.
552 (5) Contribution of other CO_2-source rocks - Beside the studied calc-silicate rock type, which is the
553 most abundant in the Himalaya and derived from a marly protolith (Fig. SM1), other CO_2-
554 source rocks occur in the GHS (see Rolfo et al., 2017 for a review). These CO_2-source rocks
555 mostly include calc-silicate –bearing metapelites (i.e. scapolite/anorthite/clinozoisite ± garnet
556 two-micas micaschists and gneisses; Rolfo et al., 2017) deriving from carbonate-rich pelites
557 (Fig. SM1). The CO_2-productivity of these lithologies is still unknown, because they have never
558 been investigated in detail; it should be in any case lower than that of the studied calc-silicate
559 rock type, because the protolith contained less calcite. Moreover, their abundance within the
560 GHS is difficult to be constrained, because these rocks are not easy to be recognised in the
561 field, resembling common metapelites (Rolfo et al., 2017). However, according to our
562 experience, their vol% cannot exceed that of the calc-silicate rock type studied in this paper.
563 Overall, the contribution of the other types of CO_2-source rocks to the total orogenic CO_2 flux
564 should be therefore minor than the CO_2 flux estimated for the studied calc-silicate type.
565 Considering the uncertainties associated with the input values (1) to (4), the metamorphic CO_2 flux
566 resulting from the studied calc-silicate type ranges between a minimum value of 1.4 Mt/yr and a
567 maximum value of 9.7 Mt/yr (Table 4). Adding the contribution of the other types of CO_2-source
568 rocks (input value 5), the maximum CO_2 flux would be 2x higher, resulting in a total metamorphic
569 CO_2 flux from the GHS ranging between 1.4 and 19.4 Mt/yr. Further studies on the CO_2-source
570 rocks derived from carbonate-rich pelitic protoliths would provide more precise constraints on the
571 CO_2 productivity of such lithologies, and consequently on the total orogenic CO_2 flux.

572 Compared to the literature data, our estimated flux of CO_2 (1.4 Mt/yr < CO_2 flux <19.4
573 Mt/yr) is slightly lower than the past CO_2 flux estimated by Kerrick and Caldeira (1999) (9 Mt/yr <
574 CO_2 flux <24 Mt/yr) using the mass loss method. The discrepancy between the two values is
575 probably due to the Kerrick and Caldeira (1999) slight over-estimation of the amount of CO_2
576 released from the CO_2-source rocks. Specifically, they assumed that: (i) the whole GHS contributed
577 to the production of CO_2 (i.e. CO_2-source rocks = 100 vol%), and that (ii) the GHS protolith was a
578 pelite with 5 wt% carbonate (i.e. ~2 wt% CO_2)[1] and all carbonate was consumed during
579 metamorphism.

580 Compared to the present-day CO_2 flux estimated on the basis of CO_2 degassed from
581 spring waters located along the MCT, our estimated flux of CO_2 (1.4 Mt/yr < CO_2 flux < 19.4 Mt/yr)
582 is lower than the estimate of Becker et al. (2008) (40 Mt/yr), but similar to that of Evans et al.
583 (2008) (8.8 Mt/yr). Becker et al. (2008) based their estimates on data from the Marsyandi basin of
584 central Nepal, which cover about ~4800 km^2, whereas the data used by Evans et al. (2008) refer to
585 the larger Narayani basin, covering ~40000 km^2 and comprising the Marsyandi basin itself.
586 According to the Evans et al. (2008) data, the contribution of the Marsyandi spring system to the
587 total flux of CO_2 is nearly one order of magnitude higher than the contributions of the other spring
588 systems of the Narayani basin. It therefore appears that the Becker et al. (2008) extrapolation to
589 the whole orogen is biased by the exceptional high CO_2 flux from the Marsyandi basin, whereas
590 the estimate by Evans et al. (2008) probably approximates better the contribution of the majority
591 of the spring systems of the Himalaya. The similarity between our estimated flux of CO_2 and that
592 actually measured from spring waters thus suggests that CO_2-producing processes similar to those
593 described in the present work still occur along the active Himalayan orogen (e.g. Girault et al.,
594 2014).

[1] Note that although in the Kerrick and Caldeira's paper a pelite with 5 wt% CO_2 (instead of 5 wt% carbonate) was mentioned as GHS protolith (which would correspond to 12.5 wt% carbonate), the authors explicitly referred to the Bickle's paper (Bickle, 1996) in which a pelite with 5 wt% carbonate was considered.

To our knowledge, this is the first time that CO_2-producing metamorphic processes occurring during an orogenic event have been fully characterized in term of P-T conditions, time, duration and amounts of CO_2 produced. Although the volumes of the CO_2-source rocks involved in such processes could be potentially better constrained in the future, we suggest that these metamorphic CO_2 fluxes should be considered in any future attempts of estimating the global budget of non-volcanic carbon fluxes from the lithosphere (e.g. Morner and Etiope, 2002).

ACKNOWLEDGMENTS

Carl Spandler (James Cook University, Australia) and Allen Kennedy (Curtin University, Australia) are kindly acknowledged for providing the MKED1 and OLT1 titanite samples. A. Skelton, A. Galy and an anonymous reviewer provided constructive comments on an earlier version of this paper. M. Kohn and A. Skelton are gratefully acknowledged for their careful and constructive reviews which significantly improve the manuscript. The instrument used to obtain the SEM-EDS data was acquired thanks to a grant from the Compagnia di San Paolo, Torino. The study was supported by the University of Torino (Ricerca Locale, ex-60% - 2014, 2015 funds) and Compagnia di San Paolo (University of Torino, Call 1, Junior PI Grant: TO_Call1_2012_0068), by the Italian Ministry of University and Research (PRIN 2011: 2010PMKZX7) and by Ev-K2-CNR (SHARE Project). The financial support of European Research Council for the Consolidator Grant ERC-2013-383 CoG Proposal No. 612776 — CHRONOS (DP) is also acknowledged.

614 **REFERENCES**

615 Ashley, K.T., Law, R.D., 2015. Modeling prograde TiO_2 activity and its significance for Ti-in-quartz
616 thermobarometry of pelitic metamorphic rocks. Contribution to Mineralogy and Petrology 169,
617 23.

618 Becker, J.A., Bickle, M.J., Galy, A., Holland, T.J.B., 2008. Himalayan metamorphic CO_2 fluxes:
619 Quantitative constraints from hydrothermal springs. Earth and Planetary Science Letters 265,
620 616–629.

621 Bickle, M.J., 1996. Metamorphic decarbonation, silicate weathering and the long-term carbon
622 cycle. Terra Nova 8, 270–276.

623 Bordet, P., 1961. Recherches geologiques dans l'Himalaya du Nepal, region du Makalu. Paris,
624 Centre National de la Recherche Scientifique.

625 Bucher, K., Grapes, R., 2011. Petrogenesis of metamorphic rocks. Springer.

626 Cherniak, D.J., 2006. Zr diffusion in titanite. Contribution to Mineralogy and Petrology 152, 639–
627 647.

628 Chew, D.M., Petrus, J.A., Kamber, B.S., 2016. U–Pb LA–ICPMS dating using accessory mineral
629 standards with variable common Pb. Chemical Geology 363, 185–199.

630 Colchen, M., Le Fort, P., Pêcher, A., 1986. Notice explicative de la carte géologique Annapurna–
631 Manaslu–Ganesh (Himalaya du Népal) au 1:200000e (bilingual: French–English), CNRS, Paris.

632 Connolly, J.A.D., 1990. Multivariable phase diagrams: an algorithm based on generalize
633 thermodynamics. American Journal of Science 290, 666–718.

634 Connolly, J.A.D., 2009. The geodynamic equation of state: what and how. Geochemistry,
635 Geophysics, Geosystems 10, Q10014.

636 Connolly, J.A.D., Trommsdorff, V., 1991. Petrogenetic grids for metacarbonate rocks: pressure–
637 temperature phase-diagrams for mixed-volatile systems. Contribution to Mineralogy and
638 Petrology 108, 93–105.
639 Corrie SL, Kohn MJ. 2011. Metamorphic history of the central Himalaya, Annapurna region, Nepal,
640 and implications for tectonic models. Geological Society of American Bulletin 123, 1863–79.
641 Corrie, S.L., Kohn, M.J., 2011. Metamorphic history of the central Himalaya, Annapurna region,
642 Nepal, and implications for tectonic models. Geological Society of American Bulletin 123, 1863–
643 1879.
644 Cossio, R., Borghi, A., Ruffini, R., 2002. Quantitative modal determination of geological samples
645 based on X-ray multielemental map acquisition. Microscopy and Microanalysis 8, 139–149.
646 Cottle, J.M., Waters, D.J., Riley, D., Beyssac, O., Jessup, M.J., 2011. Metamorphic history of the
647 South Tibetan Detachment System, Mt. Everest region, revealed by RSCM thermometry and
648 phase equilibria modelling. Journal of Metamorphic Geology 29, 561–582.
649 Diener, J.F.A., Powell, R., 2012. Revised activity-composition models for clinopyroxene and
650 amphibole. Journal of Metamorphic Geology 30, 131–142.
651 Evans, K.A., 2011. Metamorphic carbon fluxes: how much and how fast? Geology 39, 95–96.
652 Evans, M.J., Derry, L.A., France-Lanord, C., 2008. Degassing of metamorphic carbon dioxide from
653 the Nepal Himalaya. Geochemistry, Geophysics, Geosystems 9, Q04021.
654 Fettes D., Desmons J., 2007. Metamorphic Rocks: A Classification and Glossary of Terms.
655 Cambridge University Press.
656 Franz, G., Spear, F.S., 1985. Aluminous titanite from the Eclogite Zone, south central Tauern
657 Window, Austria. Chemical Geology 50, 33-46.
658 Frost, B.R., Chamberlain, K.R., Schumacher, J.C., 2000. Sphene (titanite): phase relations and role
659 as a geochronometer. Chemical Geology 172, 131–148.

660 Gaillardet, J., Galy, A., 2008. Himalaya-carbon sink or source? Science 320, 1727–1728.
661 Gansser, A., 1964. Geology of the Himalayas. London, Wiley Interscience.
662 Gao, X. Y., Zheng, Y.F., Chen, Y.X., Guo, J., 2012. Geochemical and U-Pb age constraints on the
663 occurrence of polygenetic titanites in UHP metagranite in the Dabie orogen, Lithos 136–139, 93–
664 108.
665 Girault, F., Bollinger, L., Bhattarai, M., Koirala, B.P., France-Lanord, C., Rajaure, S., Gaillardet, J.,
666 Fort, M., Sapkota, S.N., Perrier, F., 2014. Large-scale organization of carbon dioxide discharge in
667 the Nepal Himalayas. Geophysical Research Letters 41, 6358–6366.
668 Goscombe, B., Gray, D., Hand, M., 2006. Crustal architecture of the Himalayan metamorphic front
669 in eastern Nepal. Gondwana Research 10, 232–255.
670 Greenwood, H.J., 1975. Buffering of pore fluids by metamorphic reactions. American Journal of
671 Science 275, 573–593.
672 Groppo, C., Rolfo, F., Castelli, D., Connolly, J.A.D., 2013. Metamorphic CO_2 production from calc-
673 silicate rocks via garnet-forming reactions in the CFAS-H_2O-CO_2 system. Contribution to
674 Mineralogy and Petrology 166, 1655–1675.
675 Groppo, C., Rolfo, F., Castelli, D., Mosca, P., 2017. Metamorphic CO_2 production in collisional
676 orogens: petrologic constraints from phase diagram modeling of Himalayan, scapolite-bearing,
677 calc-silicate rocks in the NKC(F)MAS(T)-HC system. Journal of Petrology 58, 53–84.
678 Hayden, L.A., Watson, E.B., Wark, D.A., 2008. A thermobarometer for sphene (titanite).
679 Contribution to Mineralogy and Petrology 155, 529–540.
680 He, D., Webb, A.A.G., Larson, K.P., Martin, A.J., Schmitt, A.K., 2015. Extrusion vs. duplexing models
681 of Himalayan mountain building. 3: duplexing dominates from the Oligocene to Present.
682 International Geological Reviews 57, 1–27.

683 Holland, T.J.B., Powell, R., 1998. An internally consistent thermodynamic data set for phases of
684 petrologic interest. Journal of Metamorphic Geology 16, 309–343.
685 Iaccarino, S., Montomoli, C., Carosi, R., Massonne, H.-J., Langone, A., Visonà, D., 2015. Pressure–
686 temperature–time–deformation path of kyanite-bearing migmatitic paragneiss in the Kali
687 Gandaki valley (Central Nepal): Investigation of Late Eocene–Early Oligocene melting processes.
688 Lithos 231, 103–121.
689 Kennedy, A.K., Kamo, S.L., Nasdala, L., Timms, N.E., 2010. Grenville skarn titanite: potential
690 reference material for SIMS U-Th-Pb analysis. Canadian Mineralogist 48, 1423–1443.
691 Kerrick, D.M., Caldeira, K., 1993. Paleoatmospheric consequences of CO_2 released during early
692 Cenozoic regional metamorphism in the Tethyan orogen. Chemical Geology 108, 201–230.
693 Kerrick, D.M., Caldeira, K., 1998. Metamorphic CO_2 degassing from orogenic belts. Chemical
694 Geology 145, 213–232.
695 Kerrick, D.M., Caldeira, K., 1999. Was the Himalayan orogen a climatically significant coupled
696 source and sink for atmospheric CO_2 during the Cenozoic? Earth and Planetary Science Letters
697 173, 195–203.
698 Kohn, M.J., 2008. PTt data from central Nepal support critical taper and repudiate large-scale
699 channel flow of the Greater Himalayan Sequence. Geological Society of American Bulletin 120,
700 259–273.
701 Kohn, M.J., 2014. Himalayan metamorphism and its tectonic implications. Annual Review of Earth
702 and Planetary Sciences 42, 381–419.
703 Kohn, M.J., 2016. Metamorphic chronology - a tool for all ages: Past achievements and future
704 prospects. Ameriucan Mineralogist 101, 25–42.

Kohn, M.J., 2017. Titanite petrochronology, in: Kohn, M.J., Engi, M. and Lanari, P. (Eds.), Petrochronology: Methods and Applications, Reviews in Mineralogy and Geochemistry 83, pp. 419-417.

Kohn, M.J., Corrie, S.L., 2011. Preserved Zr-temperatures and U–Pb ages in high-grade metamorphic titanite: Evidence for a static hot channel in the Himalayan orogen. Earth and Planetary Science Letters 311, 136–143.

Kohn, M.J., Wieland, M. S., Parkinson, C.D., Upreti, B. N., 2004. Miocene faulting at plate tectonic velocity in the central Himalaya, Nepal. Earth and Planetary Science Letters 228, 299–310.

Kohn, M.J., Wieland, M., Parkinson, C.D., Upreti, B.N., 2005. Five generation of monazite in Langtang gneisses: implication for chronology of the Himalayan metamorphic core. Journal of Metamorphic Geology 23, 399–406.

Kuhn, B.K., Reusser, E., Powell, R., 2005. Metamorphic evolution of calc-schists in the Central Alps, Switzerland. Schweizerische Mineralogische und Petrographische Mitteilungen 85, 175–190.

Le Fort, P., 1975. Himalaya, the collided range: present knowledge of the continental arc. American Journal of Science 275A, 1–44.

Leloup, P.H., Liu, X., Mahéo, G., Paquette, J.-L., Arnaud, N., Aubray, A., Liu, X., 2015. New constraints on the timing of partial melting and deformation along the Nyalam section (central Himalaya): implications for extrusion models, in: Mukherjee, S., Carosi, R., van der Beek, B.K., and Robinson, D.M. (Eds.), Tectonics of the Himalaya, Geological Society of London Special Publication 412, pp. 131–175.

Long, S.L., McQuarrie, N., Tobgay, T., Grujic, D., 2011. Geometry and crustal shortening of the Himalayan fold-thrust belt, eastern and central Bhutan. GSA Bulletin 123, 1427–1447.

727 Longerich, H.P., Jackson, S.E., Günther, D., 1996. Laser ablation inductively coupled plasma mass
728 spectrometric transient signal data acquisition and analyte concentration calculation. Journal of
729 Analytical Atomic Spectrometry 11, 899–904.
730 Ludwig, K.K., 2001. Isoplot / Ex Version 2.49. A Geochronological Toolkit for Microsoft Excel.
731 Berkeley Geochronology Centre, Special Publication, Berkeley.
732 Martin, A.J., Ganguly, J., De Celles, P.G., 2010. Metamorphism of Greater and Lesser Himalayan
733 rocks exposed in the Modi Khola valley, central Nepal. Contribution to Mineralogy and Petrology
734 159, 203–223.
735 Mörner, N.A., Etiope, G., 2002. Carbon degassing from the lithosphere. Global and Planetary
736 Change 33, 185–203.
737 Newton, R.C., Charlu, T.V., Kleppa, O.J., 1980. Thermochemistry of the high structural state
738 plagioclases. Geochimica and Cosmochimica Acta 44, 933–941.
739 Paton, C., Hellstrom, J., Paul, B., Woodhead, J., Hergt, J., Kosler, J., Fonneland, H., Sylvester, P.,
740 Tubrett, M., Pedersen, R., Jackson, S.E., Pearson, N.J., Griffin, W.L., Belousova, E.A., Jackson, S.E.,
741 Longerich, H.P., Dunning, G.R., Freyer, B.J., Ulrich, T., Kamber, B.S., Jugo, P.J., Tinkham, D.K.,
742 Woodhead, J.D., Hellstrom, J., Hergt, J.M., Greig, A., Maas, R., Paton, C., Woodhead, J., Hergt, J.,
743 Phillips, D., Shee, S., Bizzarro, M., Paton, C., Larsen, K., Schiller, M., Trinquier, A., Ulfbeck, D.,
744 Paton, C., Woodhead, J.D., Hellstrom, J.C., Hergt, J.M., Greig, A., Maas, R., Hampel, F.R.,
745 Rousseeuw, P.J., Croux, C., Reinsch, C., Craven, P., Wahba, G., 2011. Iolite: Freeware for the
746 visualisation and processing of mass spectrometric data. Journal of Analytical Atomic
747 Spectrometry 26, 2508-2518.
748 Pearce, N.J.G.G., Perkins, W.T., Westgate, J.A., Gorton, M.P., Jackson, S.E., Neal, C.R., Chenery,
749 S.P., 1997. A compilation of new and published major and trace element data for NIST SRM 610

and NIST SRM 612 Glass Reference Materials. Geostandards and Geoanalytical Research 21, 115–144.

Petrelli, M., Morgavi, D., Vetere, F., Perugini, D., 2016. Elemental imaging and petro-volcanological applications of an improved Laser Ablation Inductively Coupled Quadrupole Plasma Mass Spectrometry. Periodico di Mineralogia 85, 25-39.

Rapa, G., Groppo, C., Mosca, P., Rolfo, F., 2016. Petrological constraints on the tectonic setting of the Kathmandu Nappe in the Langtang-Gosainkund-Helambu regions, Central Nepal Himalaya. Journal of Metamorphic Geology 34, 999–1023.

Rolfo, F., Groppo, C., Mosca, P., 2017. Metamorphic CO_2 production in calc-silicate rocks from the eastern Himalaya. Italian Journal of Geosciences, doi: 10.3301/IJG.2015.36.

Rolfo, F., Groppo, C., Mosca, P., Ferrando, S., Costa, E., Kaphle, K.P., 2015. Metamorphic CO_2 degassing in the active Himalayan orogen: exploring the influence of orogenic activity on the long-term global climate changes, in: Lollino, G., Manconi, A., Clague, J., Shan, W., Chiarle, M. (Eds.), Engineering Geology for Society and Territory 1, Springer, pp. 21-25.

Selverstone, J., Gutzler, D.S., 1993. Post-125 Ma carbon storage associated with continent–continent collision. Geology 21, 885–888.

Skelton, A., 2011. Flux rates for water and carbon during greenschist facies metamorphism. Geology 39, 43–46.

Skelton, A., 2013. Is orogenesis a net sink or source of atmospheric CO_2? Geology Today 29, 102–107.

Spandler, C., Hammerli, J., Sha, P., Hilbert-Wolf, H., Hu, Y., Roberts, E., Schmitz, M., 2016. MKED1: A new titanite standard for in situ analysis of Sm–Nd isotopes and U–Pb geochronology. Chemical Geology 425, 110–126.

773 Spencer, K.J., Hacker, B.R., Kylander-Clark, A.R.C., Andersen, T.B., Cottle, J.M., Stearns, M.A.,
774 Poletti, J.E., Seward, G.G.E., 2013. Campaign-style titanite U–Pb dating by laser-ablation ICP:
775 Implications for crustal flow, phase transformations and titanite closure. Chemical Geology 341,
776 84–101.
777 Stacey, J.S., Kramers, J.D, 1975. Approximation of terrestrial lead isotope evolution by a two-stage
778 model. Earth and Planetary Sceince Letters 26, 207-221.
779 Stearns, M.A., Hacker, B.R., Ratschbacher, L., Rutte, D., Kylander-Clark, A.R.C., 2015. Titanite
780 petrochronology of the Pamir gneiss domes: Implications for middle to deep crust exhumation
781 and titanite closure to Pb and Zr diffusion. Tectonics 34, 784–802.
782 Tajcmanova, L., Connolly, J.A.D., Cesare, B., 2009. A thermodynamic model for titanium and ferric
783 iron solution in biotite. Journal of Metamorphic Geology 27, 153–165.
784 Walters, J.B., Kohn M.J., in press. Protracted thrusting followed by late rapid cooling of the Greater
785 Himalayan Sequence, Annapurna Himalaya, Central Nepal: Insights from titanite
786 petrochronology. Journal of Metamorphic Geology 35, 897–917.
787 Wang, J-M., Zhang, J-J., Liu, K., Wang, X-X., Rai, S., Scheltens, M., 2016. Spatial and temporal
788 evolution of tectonometamorphic discontinuities in the Central Himalaya: Constraints from P-T
789 paths and geochronology. Tectonophysics 679, 41-60.
790 Warren, C.J., Grujic, D., Cottle J.M., Rogers, N.W., 2012. Constraining cooling histories: rutile and
791 titanite chronology and diffusion modelling in NW Bhutan. Journal of Metamorphic Geology 30,
792 113-130.
793 Whitney, D.L., Evans, B.W., 2010. Abbreviations for names of rock-forming minerals. American
794 Mineralogist 95, 185-187.

795 Yakymchuk, C., Godin, L., 2012. Coupled role of deformation and metamorphism in the
796 construction of inverted metamorphic sequences: an example from far-northwest Nepal. Journal
797 of Metamorphic Geology, 30, 513–535.
798

Figure captions

Fig. 1 - (a) Geological sketch map of the central–eastern Nepal Himalaya, showing major tectono-metamorphic units (modified from Goscombe and Hand, 2000; He et al., 2015; Wang et al., 2016 and based on our own data). The white rectangle indicates the location of (b). 1: Siwalik deposits; 2: Lesser Himalayan Sequence; 3: Lower Greater Himalayan Sequence; 4: Upper Greater Himalayan Sequence; 5: Tethyan Sedimentary Sequence. MFT, Main Frontal Thrust; MBT, Main Boundary Thrust; MCT: Main Central Thrust; STDS: South Tibetan Detachment System. The inset locates the study area in the framework of the Himalayan chain. **(b)** Geological map of the Langtang and Gosainkund–Helambu regions in central Nepal Himalaya (modified from Rapa et al., 2016) and location of the studied sample 14-53c (yellow star). The white stars indicate the location of L-GHS samples dated by Kohn et al. (2004, 2005) (monazite U-Pb ages), and discussed in the text. GSZ, Galchi Shear Zone (from He et al., 2015); MCT, Main Central Thrust; LT, Langtang Thrust. **(c)** Outcrop images of the ~2 m -thick calc-silicate level from which the studied sample 14-53c was collected. The calc-silicate level shows a banded structure, being characterized by dm-thick layers with different mineral assemblages: (a) quartz + clinopyroxene + calcic plagioclase; (b) garnet + calcic plagioclase + clinopyroxene + epidote; (c) quartz + clinopyroxene + calcic plagioclase + K-feldspar + scapolite ± calcite; (d) quartz + garnet + scapolite + clinopyroxene + calcic plagioclase.

Fig. 2 – Processed micro-XRF map of the whole thin section 14-53c, with distinction of Cal-rich and Cal-poor domains. Note that the fine-grained nature of epidote hampered its discrimination in the micro-XRF map. Calcite-poor domains consist of (vol%): quartz (45%), K-feldspar (15%), clinopyroxene (11%), plagioclase (10%), scapolite (9%), zoisite (4%), biotite (4%), titanite (2%), minor calcite (<<1%) and accessory tourmaline. Calcite-rich domains are characterized by higher modal amounts of calcite, scapolite and plagioclase and lower amounts of K-feldspar, quartz and

822 biotite (quartz: 34%; scapolite: 17%; plagioclase: 14%; clinopyroxene: 14%; K-feldspar: 9%; zoisite:
823 6%; calcite: 1%; biotite: 3%; titanite: 2%).

824 **Fig. 3** – Representative microstructures involving K-feldspar and clinopyroxene. **(a)** K-feldspar and
825 quartz inclusions in a biotite flake (Back Scattered Electron image, BSE). **(b)** K-feldspar includes
826 rounded quartz and scapolite crystals (Crossed Polarized Light: XPL). **(c)** Rounded inclusion of
827 clinopyroxene in K-feldspar (XPL). **(d)** Clinopyroxene granoblast in a Cal-rich domain (XPL). The
828 inset shows a detail of the amphibole + calcite + quartz polymineralic inclusion hosted in the
829 clinopyroxene core, with corroded and lobated margins against clinopyroxene (BSE). **(e)**
830 Clinopyroxene granoblast in a Cal-poor domain, with scapolite, titanite and quartz inclusions in the
831 rims. K-feldspar in the matrix exhibits straight contacts with it (BSE). **(f)** Rounded biotite included
832 in the clinopyroxene core in a Cal-rich domain (Plane Polarized Light: PPL).

833 **Fig. 4** – Representative microstructures involving plagioclase and scapolite. **(a)** Scapolite and
834 quartz inclusions in plagioclase, showing lobated and rounded margins against it (XPL). **(b)**
835 Plagioclase granoblast in a Cal-rich domain, including clinopyroxene, K-feldspar and quartz (XPL).
836 **(c)** Plagioclase in a Cal-poor domain, growing at the expenses of clinopyroxene (XPL). **(d)**
837 Plagioclase from a Cal-rich domain includes rounded quartz and calcite. It is replaced by an
838 aggregate of epidote + calcite at its margins (BSE). **(e)** Relict of plagioclase (bytownite) replaced by
839 scapolite (XPL). The inset highlights the corroded margins of plagioclase (BSE). **(f)** Calcite growing
840 on scapolite in a Cal-rich domain. (XPL). **(g)** Epidote + quartz + calcite symplectitic aggregate
841 growing at the expense of scapolite (retrograde microstructure) (XPL). **(h)** Detail of (g) (BSE). **(i)**
842 Plagioclase including K-feldspar and quartz, replaced by an epidote rim (retrograde
843 microstructure) in a Cal-poor domain (XPL).

844 **Fig. 5** – Representative microstructural relationships between titanite and the other rock-forming
845 minerals (BSE). a,e,f: Cal-poor domain; b,c,d: Cal-rich domain.

Fig. 6 – Compositional diagrams for scapolite, plagioclase, clinopyroxene and amphibole.

Fig. 7 – **(a)** P/T-X(CO_2) pseudosection calculated for the Cal-poor domain, in the system NCKMFAST-HC along a P/T gradient reflecting the P-T path followed by the hosting metapelites (Rapa et al., 2016; P (bar) = 20.5 T(K) – 10294). White, light- and dark-grey fields are di-, tri- and quadri-variant fields, respectively; the narrow divariant fields correspond to the univariant reactions in the corresponding P/T-X(CO_2) sections (see Fig. SM2). Dashed fields are dolomite-, garnet-, and/or chlorite-bearing fields, not relevant for this study (because these phases are not observed in the studied sample). The purple arrow approximates the P/T-X(CO_2) internally buffered fluid evolution as constrained by the relevant microstructures (see Section 5.1). The purple box constrains the Zr-in-Ttn temperatures obtained from the analysed titanite grains. **(b)** Same isobaric P/T–X(CO_2) pseudosection as in (a): the univariant and invariant equilibria relevant to the Cal-poor domain are outlined (reactions labels and colors as in Fig. SM2). Note that the univariant curves and invariant points overlap the (narrow) divariant fields and (short) univariant lines of the pseudosection. The inset shows the variation in titanite (vol%) and CO_2 (wt%) amounts along the inferred P/T-X(CO_2) path (purple arrow in (a)) and highlights the main prograde episodes of titanite growth and CO_2 production (see Section 5.2).

Fig. 8 – **(a)** Temperature-time diagram for sample 14-53c, showing gradually increasing temperatures between 28 and 19 Ma and a retrograde cooling at ~15 Ma (grey symbols refer to the retrograde titanite generation). Errors on temperatures are ± 10°C (see Section 3.4 for Discussion). **(b)** Frequency distribution of Zr-in-Ttn temperatures; the two titanite grains interpreted as retrograde are not considered, due to the uncertainties in the estimate of their temperature of crystallization. **(c)** Probability density plot for U-Pb ages (common Pb $^{207}Pb/^{206}Pb$ = 0.84); although partially overlapped, the “near peak” and “peak” titanite generations are clearly

869 distinguishable. The dotted line refers to titanite ages obtained for a higher common Pb value
870 ($^{207}Pb/^{206}Pb = 0.9$).

871 **Fig. 9 –** Inverse isochron plot of the titanite U–Pb data, plotted using ISOPLOT (Ludwig, 2001). The
872 numbers marked along the concordia line are ages in Ma. Color coded according to Zr-in-Ttn
873 temperatures (as in Fig. 8).

874 **Fig. 10** – Comparison between monazite and titanite ages from the L-GHS unit in the Langtang-
875 Gosainkund region of central Nepal (see Fig. 1b for the location of the analysed samples). **(a)**
876 Probability distribution of monazite ages from Kohn et al. (2004, 2005). **(b)** Probability distribution
877 of titanite ages (this study). Note the good match between the two sets of data, which reinforces
878 the validity of our results. Color coded as in Fig. 8.

879 **Fig. 11** – (a) Simplified tectonic map of the Himalayan-Tibetan orogen, with location of the cross-
880 sections reported in (b). Modified from He et al. (2015) and Wang et al. (2016). (b) Fourteen
881 schematic profiles across the Himalayan metamorphic core in Nepal, representing the main
882 tectono-metamorphic units, major structures, and abundance of Cpx + Kfs + Scp + Pl ± Qz ± Cal
883 calc-silicate rocks (vol%, below each profile). The profiles are constructed from detailed mapping
884 along each sections by our group (cross-sections 5 to 14; see also Goscombe et al., 2006 for cross-
885 sections 10, 12, 13, 14, and Leloup et al., 2015 for cross-section 7) and by other authors: 1:
886 Yakymchuk and Godin, 2012; 2: Iaccarino et al., 2015; 3: Martin et al., 2010; Corrie and Kohn,
887 2011; 4: Colchen et al., 1986.

888

889

Fig. 1

Click here to download high resolution image

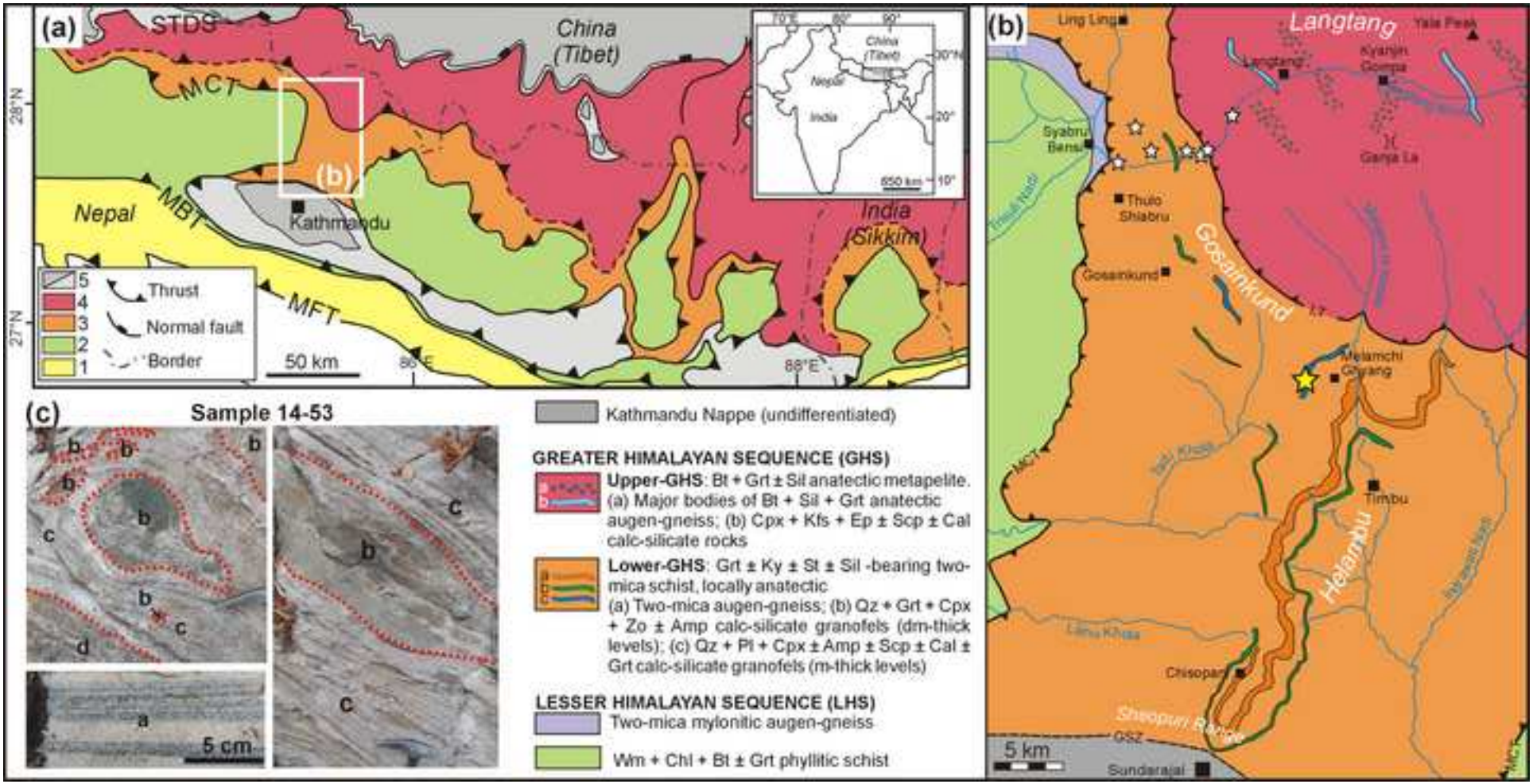

Fig. 2

Click here to download high resolution image

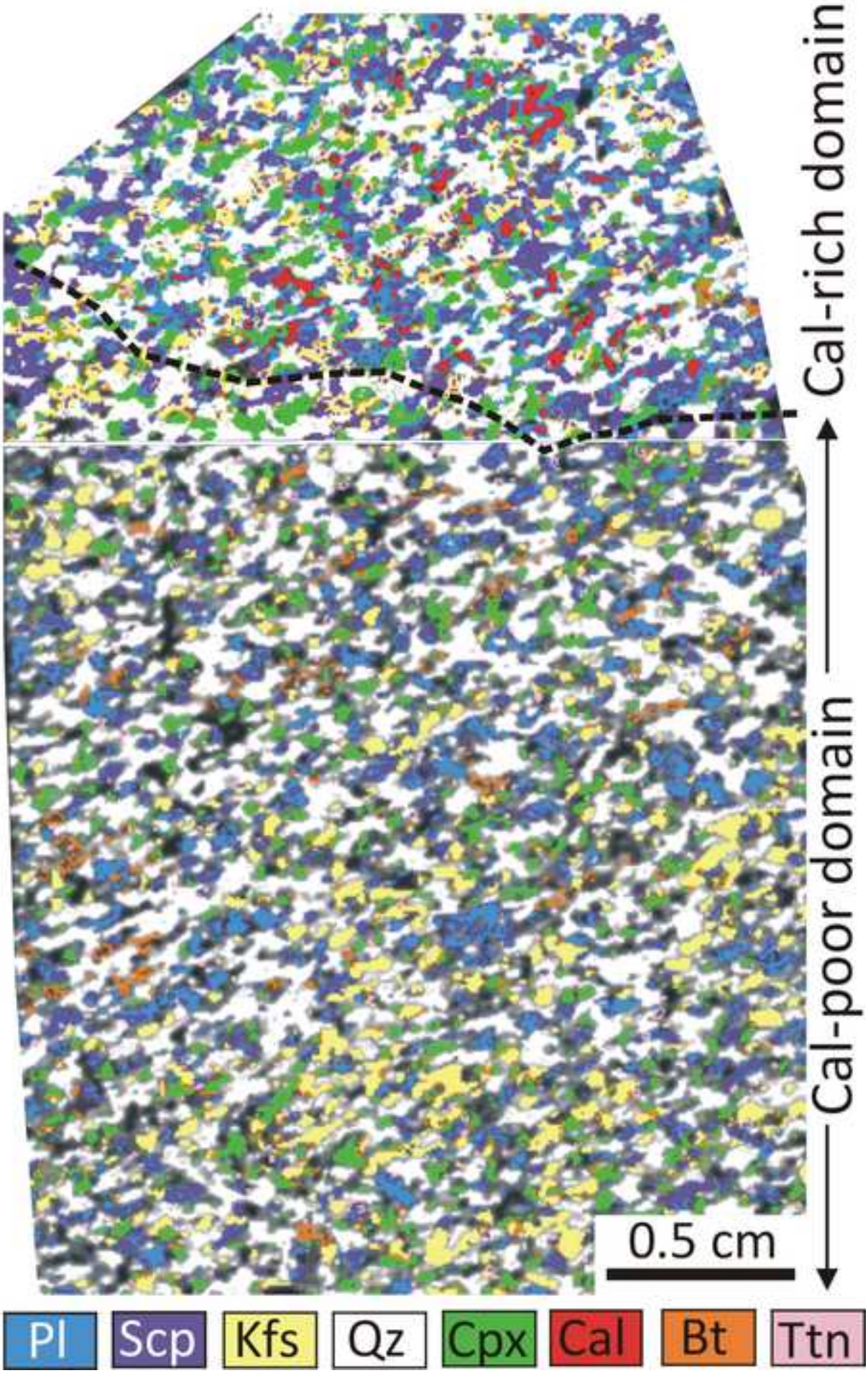

Fig. 3

Click here to download high resolution image

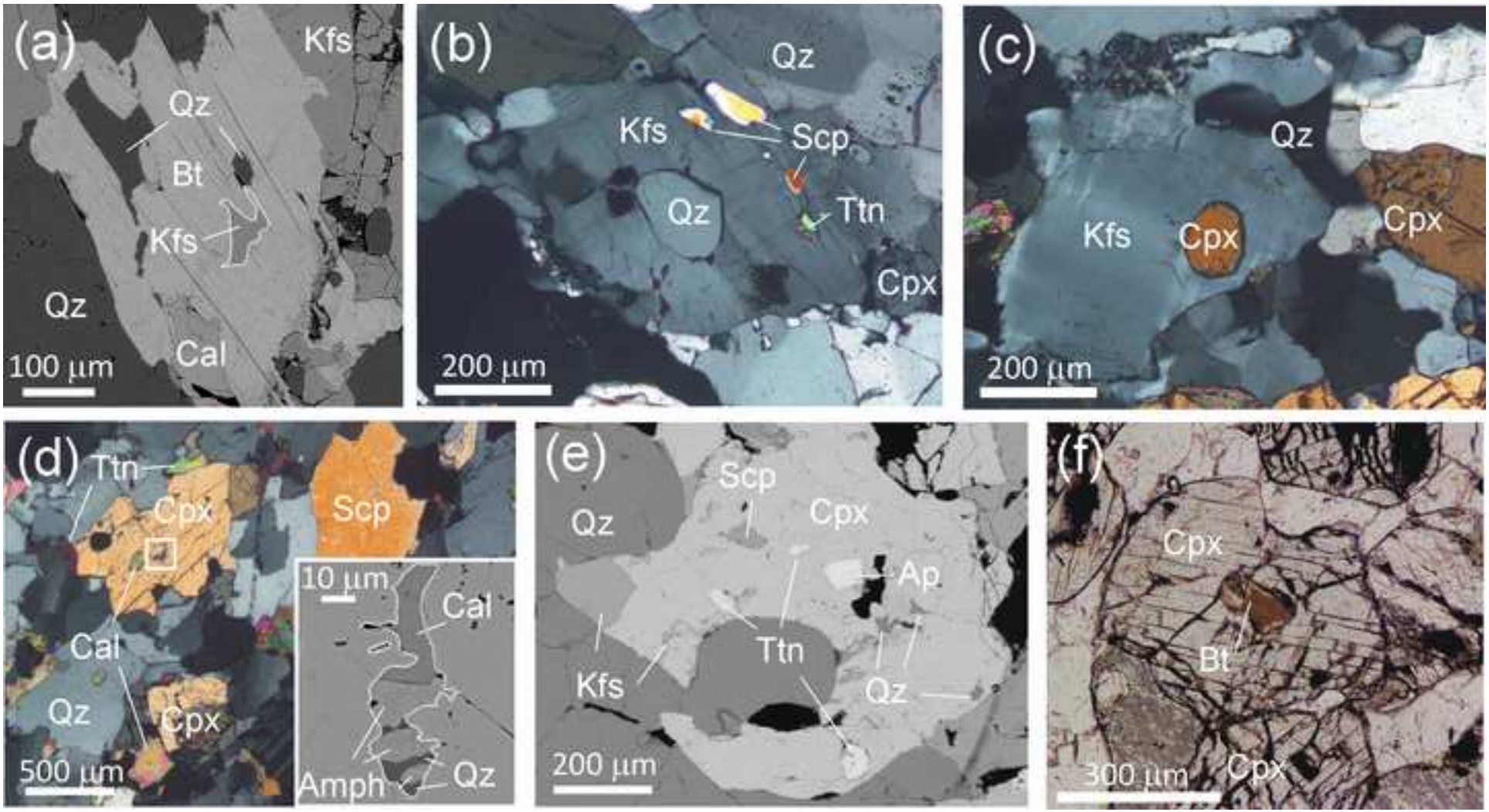

Fig. 4

Click here to download high resolution image

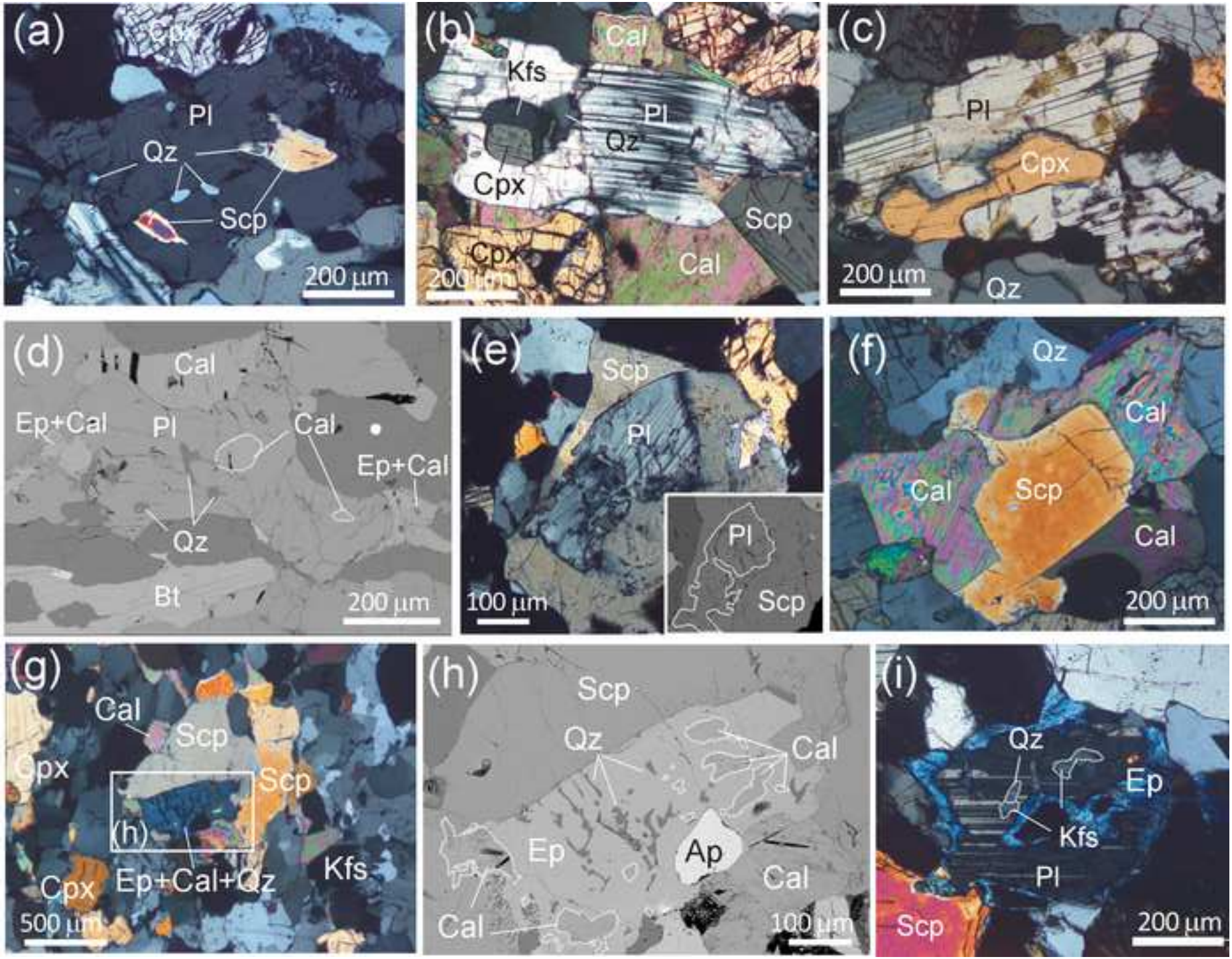

Fig. 5

Click here to download high resolution image

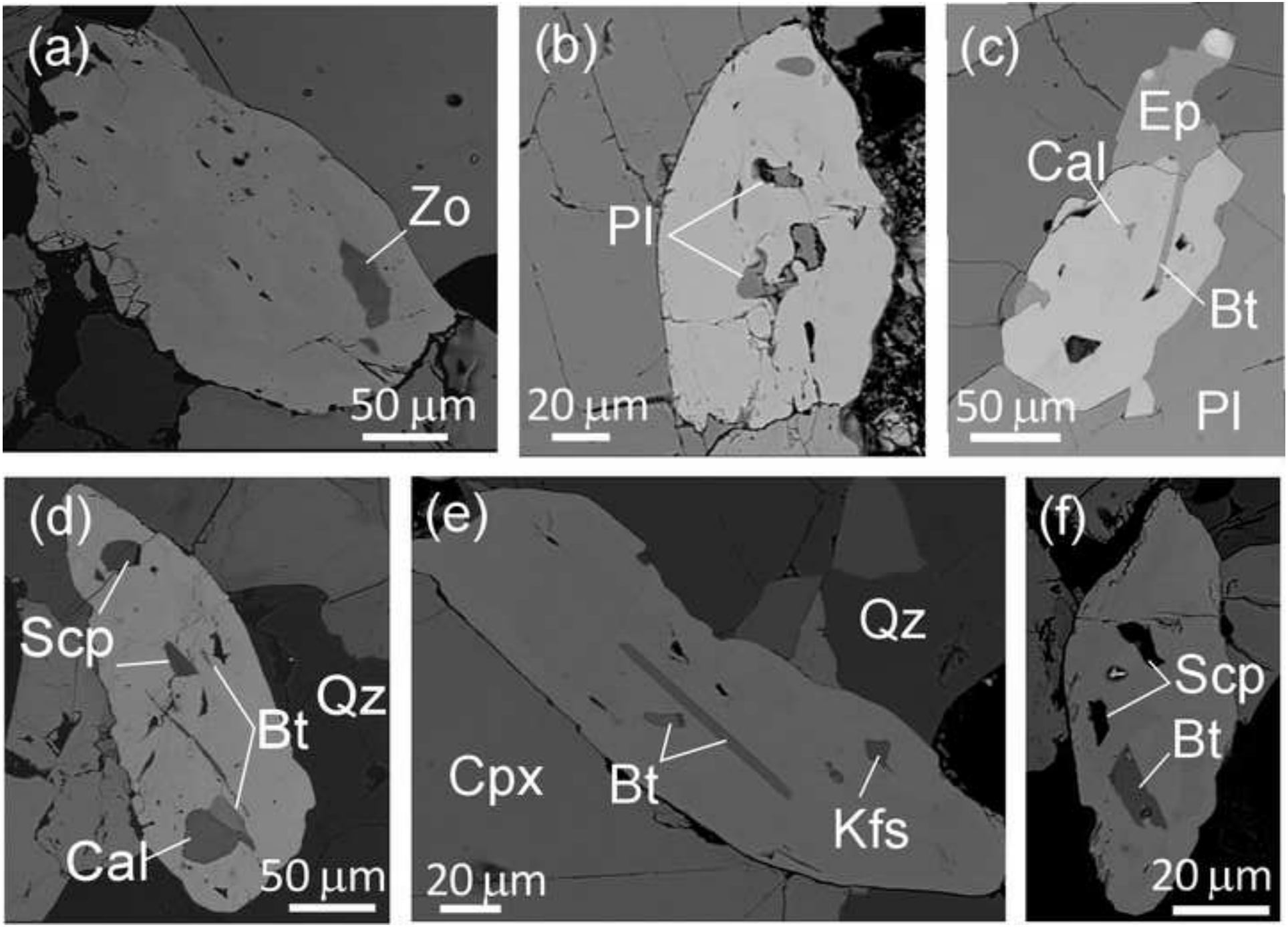

Fig. 6

Click here to download high resolution image

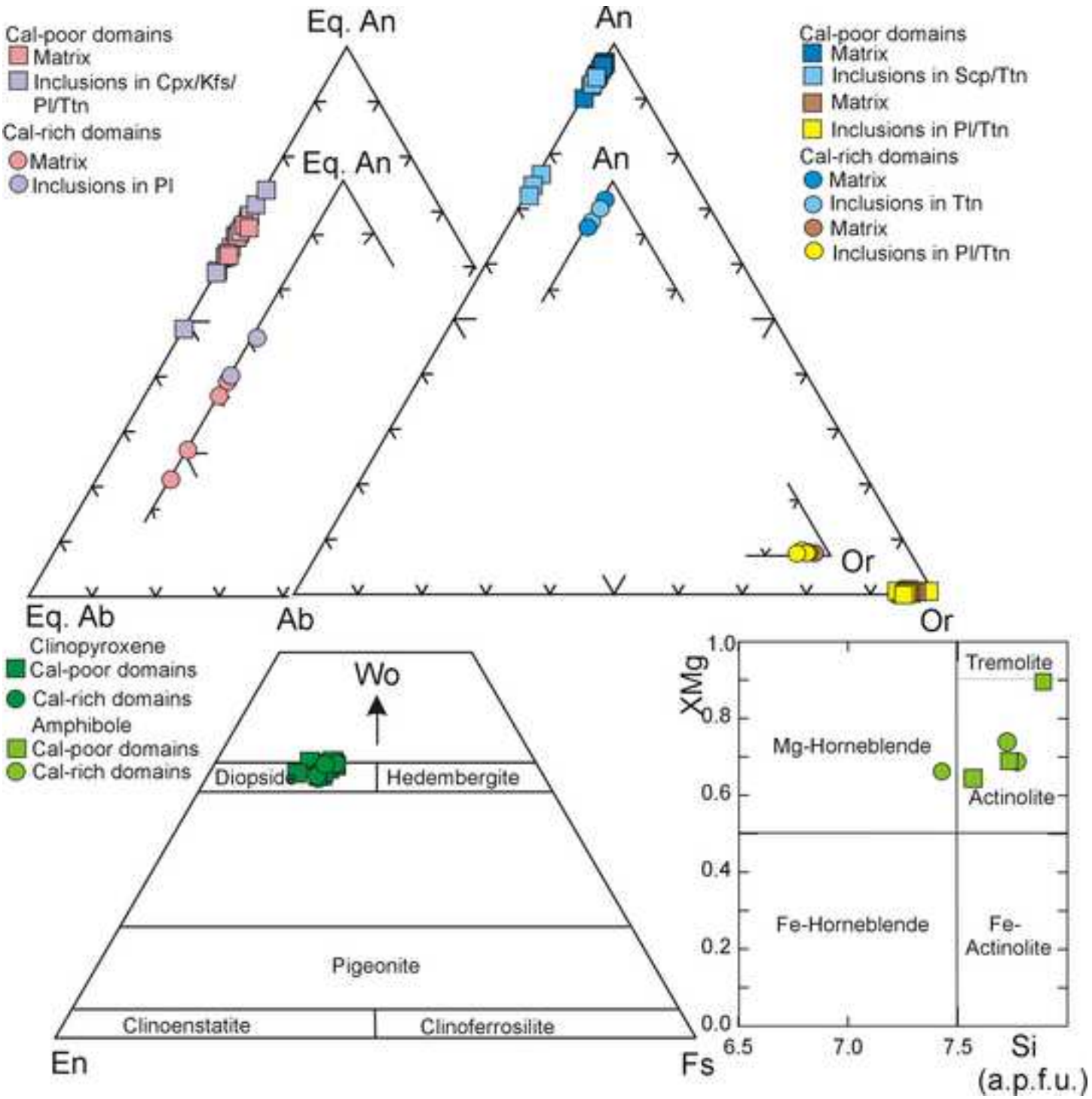

Fig. 7

Click here to download high resolution image

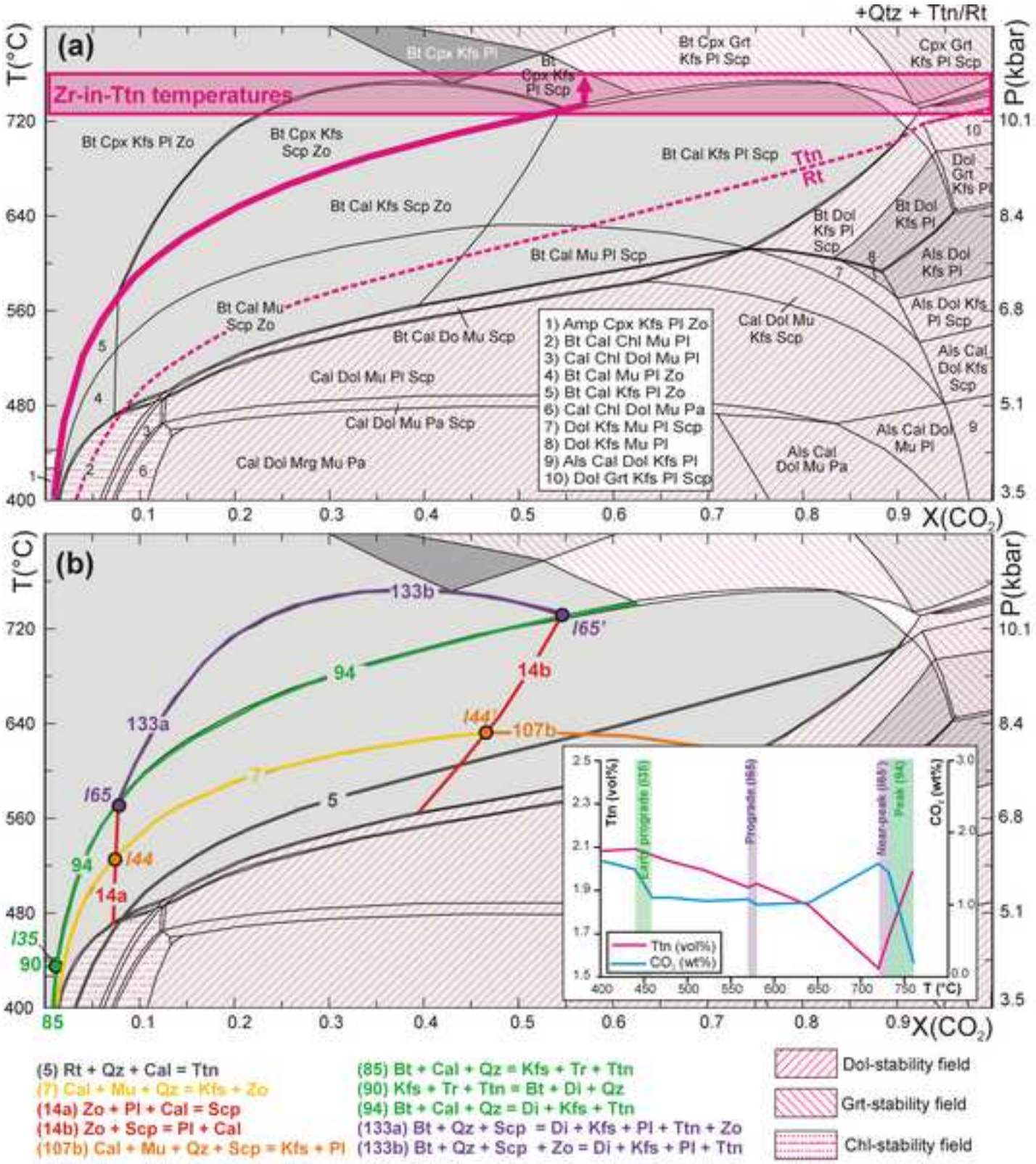

Fig. 8

Click here to download high resolution image

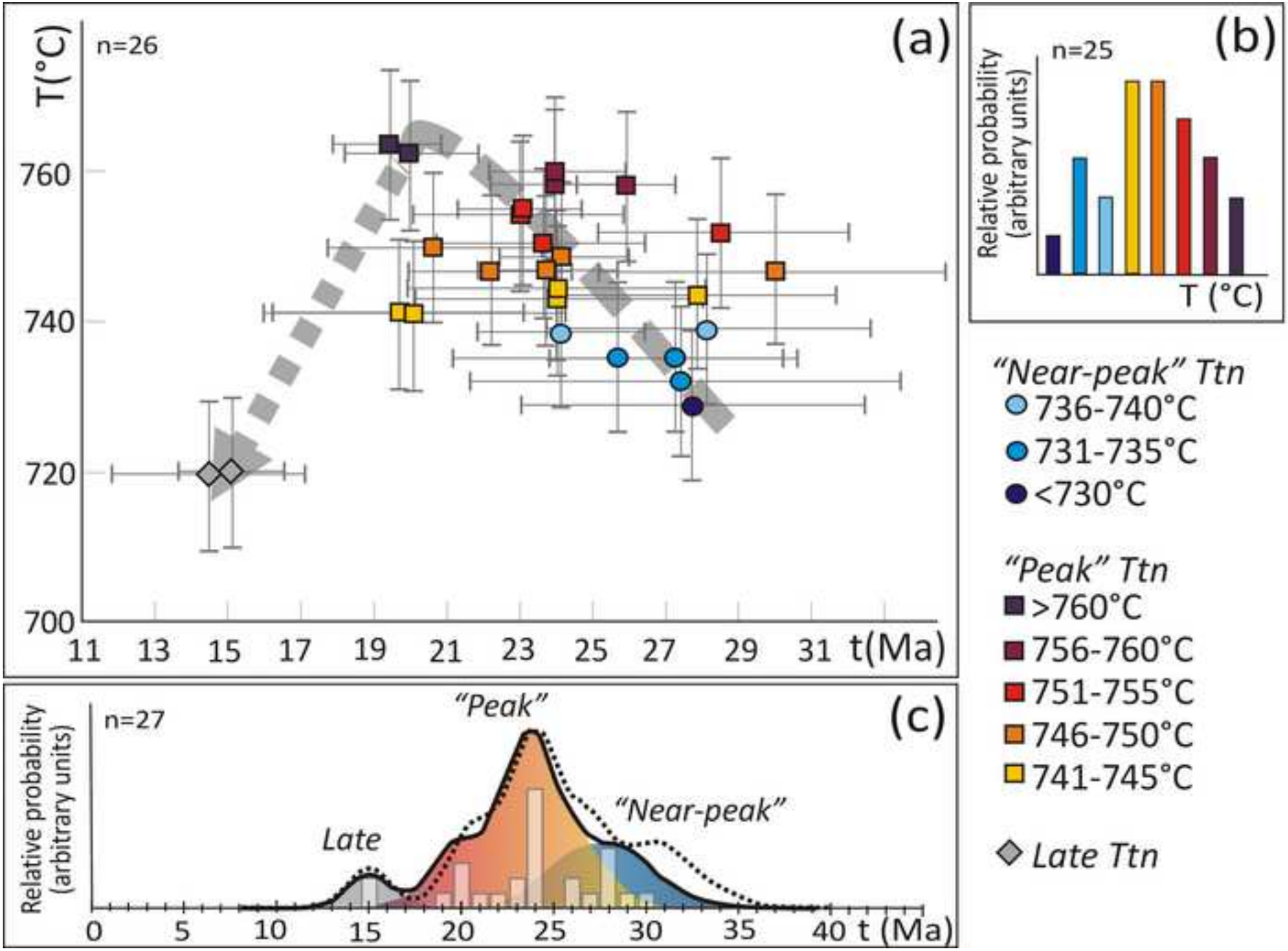

Fig. 9

Click here to download high resolution image

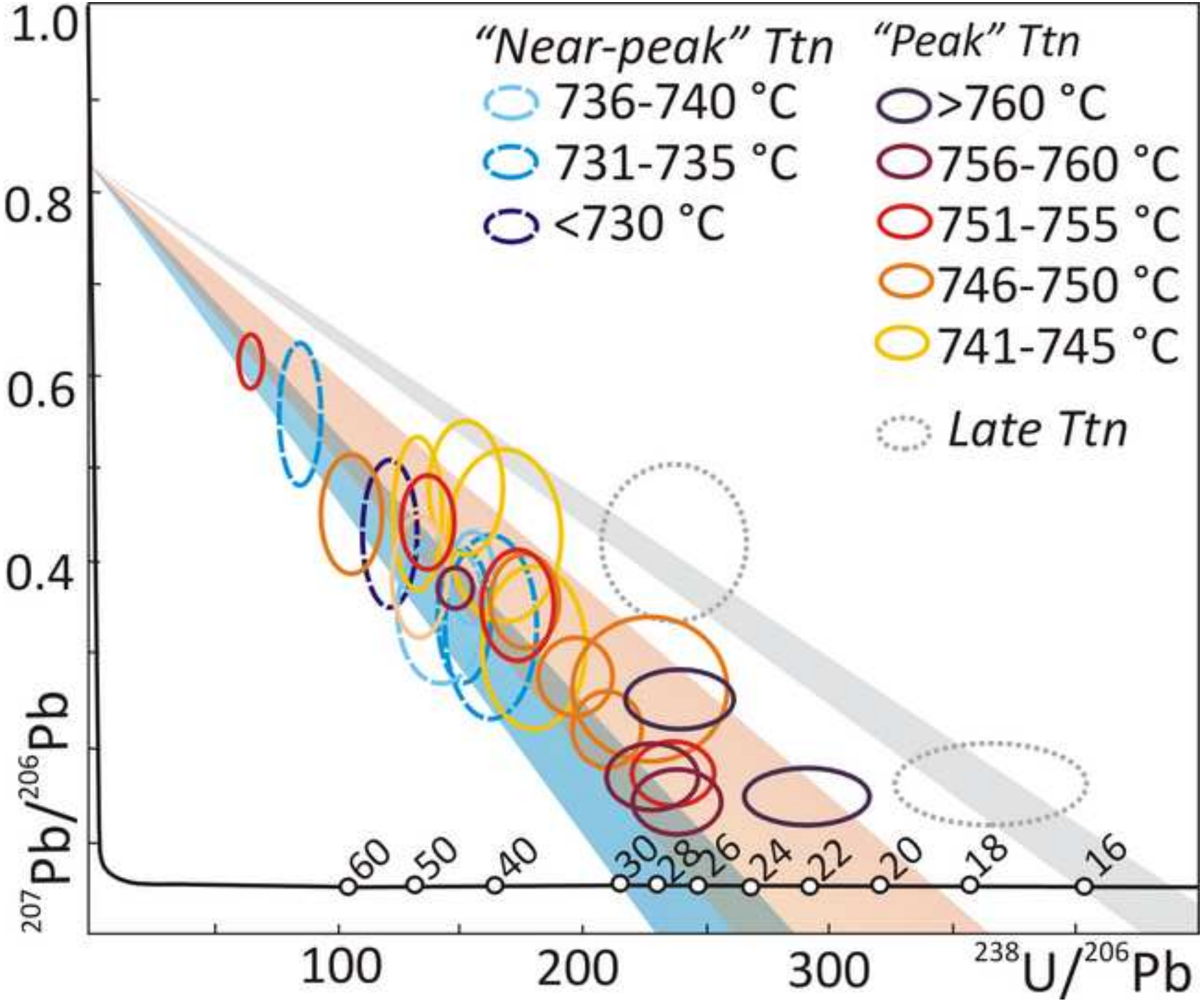

Fig. 10

Click here to download high resolution image

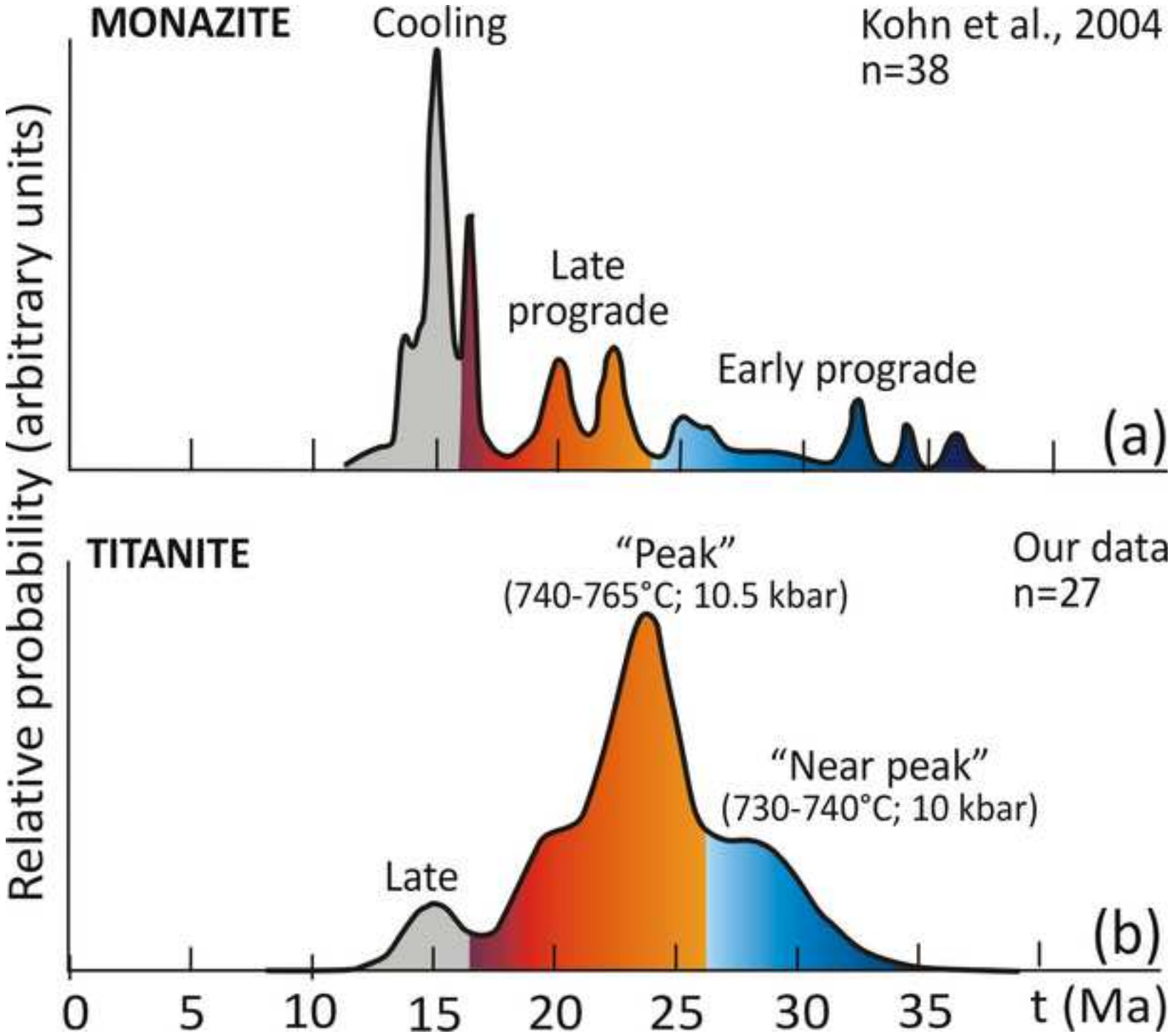

Fig. 11

Click here to download high resolution image

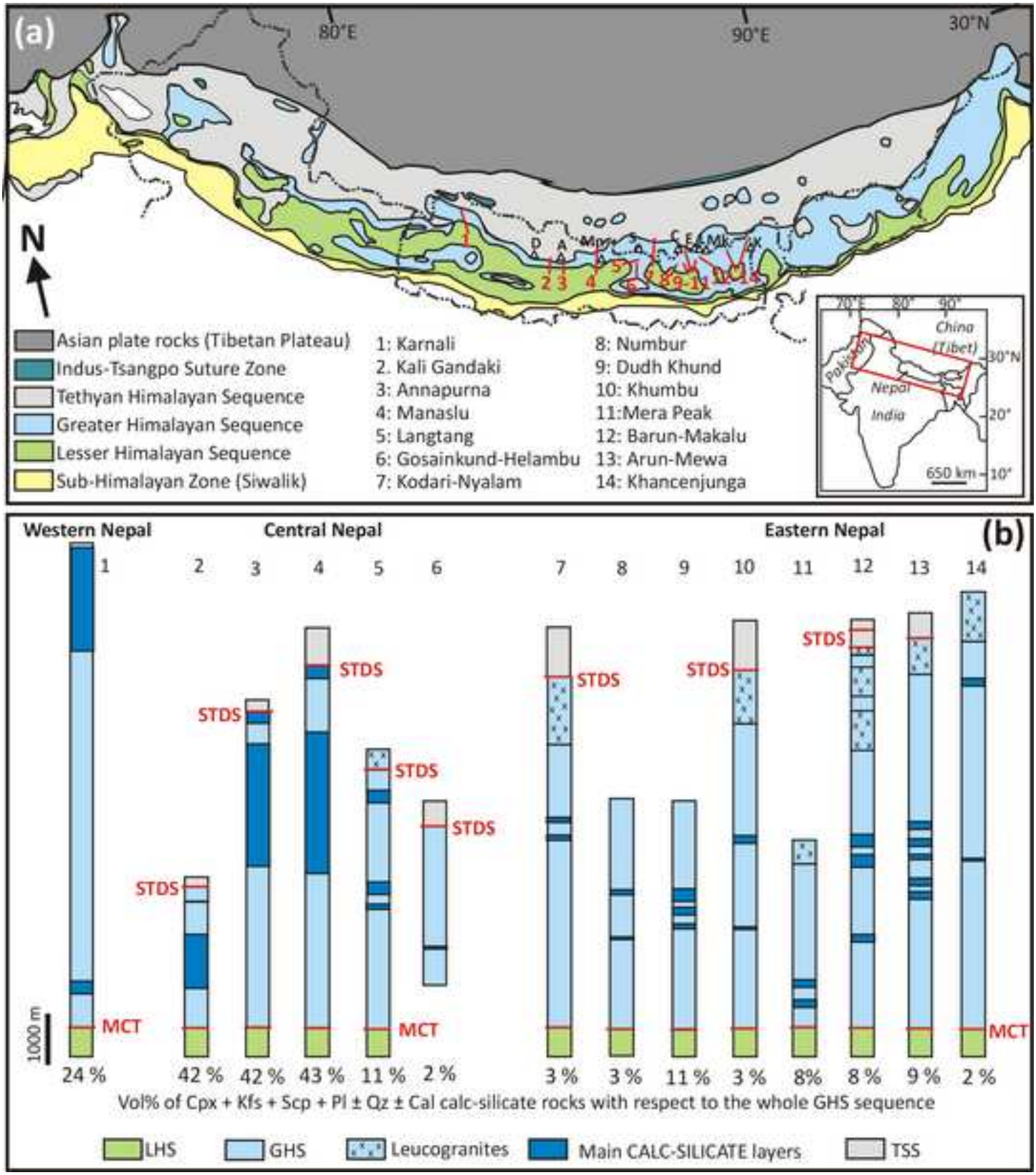

Table 1

Click here to download Table: Table 1.xlsx

Table 1.

Mineral modes and predicted amounts of titanite and CO_2

(a) Predicted vs. observed modal amount (vol%) of minerals

	Cal-poor domain		Cal-rich domain	
	Predicted at 750°C, $X(CO_2)$=0.57	Observed	Predicted at 750°C, $X(CO_2)$=0.57	Observed
Bt	3.0	4	-	3
Cal	-	-	1.8	1
Cpx	12.8	11	17.0	14
Kfs	16.1	15	10.9	9
Pl	19.1	10	22.7	14
Qz	43.5	45	31.5	34
Scp	3.5	9	14.6	17
Ttn	2.0	2	1.5	2
Zo	-	4	-	6

(b) Predicted amounts of titanite and CO_2 produced during different events

	Cal-poor domain		Cal-rich domain	
	Ttn (vol%)	CO_2 (wt%)	Ttn (vol%)	CO_2 (wt%)
early prograde	-0.1	0.50	-0.1	0.85
prograde	0.02	0.10	0.05	0.30
near-peak	0.1	0.15	0.2	0.25
peak	0.4	1.25	0.4	1.45
Total	0.4	2.0	0.6	2.9

Table 2

Click here to download Table: Table 2.xlsx

Table 2.

Bulk compositions (mol%)

	Cal-poor domain	Cal-rich domain
SiO_2	74.81	67.91
TiO_2	0.92	0.62
Al_2O_3	6.76	8.65
MgO	3.56	3.74
FeO	1.93	2.00
CaO	9.77	15.29
Na_2O	0.32	0.65
K_2O	1.93	1.15
Total	100.00	100.00

Table 3

Click here to download Table: Table 3.xlsx

Table 3.

Zirconium temperature, isotopic data and calculated ages (± 2σ) for sample 14-53c

Analysis	*a* (TiO_2)	P (GPa)	Zr (ppm)	U (ppm)	T (°C)[§]	$^{238}U/^{206}Pb$	± 2σ	$^{207}Pb/^{206}Pb$	± 2σ
"Near peak" Ttn generation									
A.1 ttn2	0.55	1	133	19	729	120.34	8.69	0.428	0.064
4.g ttn16	0.6	1	130	32	732	85.25	6.54	0.551	0.061
B.2 ttn	0.6	1	139	34	735	151.52	9.41	0.333	0.058
8.d ttn28	0.55	1	140	42	735	162.34	15.81	0.325	0.080
N.1 ttn	0.6	1	145	28	737	154.80	8.39	0.378	0.040
L.1 ttn2	0.6	1	149	29	739	143.06	14.74	0.342	0.065
"Peak" Ttn generation									
8.m ttn34	0.6	1.05	140	31	741	168.63	19.05	0.423	0.078
G.1 ttn1	0.6	1.05	142	37	742	152.91	12.63	0.471	0.061
D.1 ttn1	0.6	1.05	145	28	743	132.63	9.15	0.447	0.065
3.c ttn10	0.6	1	164	67	744	133.33	10.13	0.383	0.054
8.c ttn27	0.6	1	169	73	745	180.18	17.53	0.305	0.073
H.2 ttn	0.6	1.05	157	41	747	177.62	11.99	0.354	0.042
N.2 ttn 1	0.6	1.05	157	57	747	196.08	12.30	0.270	0.033
6.a ttn21	0.6	1	177	62	747	106.04	10.57	0.444	0.053
7.a ttn24	0.6	1	183	116	749	209.64	11.87	0.213	0.033
3.a ttn9	0.6	1.05	167	57	750	227.27	25.83	0.259	0.063
H.1 ttn2	0.6	1.05	169	63	751	136.43	8.38	0.441	0.043
F.1 ttn1	0.6	1	193	96	752	65.45	3.94	0.610	0.024
I.1 ttn2	0.6	1.05	181	82	754	173.91	12.40	0.349	0.050
4.a ttn12	0.6	1.05	183	89	755	236.97	14.04	0.167	0.030
H.1 ttn1	0.6	1.05	195	112	758	238.66	14.81	0.135	0.028
A.1 ttn	0.55	1	237	207	758	147.93	5.47	0.367	0.018
L.1 ttn1	0.6	1.05	201	104	760	227.79	15.05	0.165	0.031
E.2 ttn	0.6	1.05	211	130	762	239.81	17.25	0.247	0.028
G.1 ttn3	0.6	1.05	216	140	764	291.55	21.25	0.142	0.024
Late Ttn generation									
C.1.l ttn3	0.6	0.9	130	73	720	238.10	23.81	0.414	0.069
I.1 ttn1	0.6	0.9	133	91	721	366.30	32.20	0.155	0.037

[§]Uncertanties in T is assumed to be ±10°C.

Table 4

Click here to download Table: Table 4.xlsx

Table 4.

Sensitivity analysis for the metamorphic CO_2 flux from the Greater Himalayan Sec

Variables	Values used in this paper	Max duration of CO_2-producing process
V GHS (km^3)	5.0E+06	5.0E+06
Vol% calc-silicate rocks (%)	10	10
CO_2 productivity (Wt% CO_2)	3	3
Duration of the CO_2-producing process (Ma)	20	30
CO_2 flux* (Mt/yr)	**2.0**	**1.4**
Total CO_2 flux§ (Mt/yr)	**< 4**	**< 3**

* CO_2 flux from the studied calc-silicate rock type (i.e. derived from marly protoliths); § Total CO_2 flux
rich pelitic protoliths). Grey cells correspond to the variable parameters.

Background dataset for online publication only

Click here to download Background dataset for online publication only: Rapa et al_SUPPLEMENTARY MATERIAL.pdf